Si/Ag/C Nanohybrids with *in situ* Incorporation of Super-Small Silver Nanoparticles: Tiny Amount, Huge Impact

Shanshan Yin[1, 2†], Dong Zhao[3†], Qing Ji[1, 4], Yonggao Xia[1], Senlin Xia[5], Sophia Haussener[6], Xinming Wang[1], Meimei Wang[1], Jianzhen Ban[1, 7], Yi Zhang[1, 2], Ezzeldin Metwalli[5], Xiaoyan Wang[1, 8], Ying Xiao[1], Xiuxia Zuo[1, 8], Shuang Xie[1, 8], Kai Fang[1, 7], Suzhe Liang[1, 2], Luyao Zheng[1, 8], Bao Qiu[1], Zhaohui Yang[9], Yichao Lin[1], Liang Chen[1], Cundong Wang[2], Zhaoping Liu[1], Jin Zhu[1], Peter Müller-Buschbaum[5], and Ya-Jun Cheng[1,10*]

1. Ningbo Institute of Materials Technology and Engineering, Chinese Academy of Science, 1219 Zhongguan West Rd, Ningbo, 315201, P. R. China

2. North University of China, Shanglan Rd, Taiyuan, Shanxi Province, 030051, P. R. China

3. Max-Planck Institute for Solid State Research, Heisenbergstrasse 1, 70569 Stuttgart, Germany

4. The University of Nottingham Ningbo China, 199 Taikang East Road, Ningbo, 315100, P. R. China

5. Physik-Department, Lehrstuhl für Funktionelle Materialien, Technische Universität München, James-Franck-Str. 1, 85748 Garching, Germany

6. Laboratory of Renewable Energy Science and Engineering, Ecole Polytechnique Fédérale de Lausanne (EPFL), Station 9, 1015 Lausanne, Switzerland

7. Nano Science and Technology Institute, University of Science and Technology of China, 166 Renai Rd, Suzhou, 215123, P.R. China

8. University of the Chinese Academy of Sciences, 19 A Yuquan Rd, Shijingshan District, Beijing,

100049, P. R. China

9. Center for Soft Condensed Matter Physics and Interdisciplinary Research, Soochow University, Suzhou 215006, P. R. China

10. Department of Materials, University of Oxford, Parks Rd, OX1 3PH, Oxford, UK

† Shanshan Yin and Dong Zhao contribute equally to this work.

Email address: chengyj@nimte.ac.cn

ABSTRACT

Silicon (Si) has been regarded as one of the most promising anodes for next generation lithium ion batteries (LIBs) due to its exceptional capacity, appropriate voltage profile, and reliable operation safety. However, poor cyclic stability and moderate rate performance have been critical drawbacks to hamper the practical application of Si-based anodes. It has been one of the central issues to develop new strategies to improve the cyclic and rate performance of the Si-based lithium-ion battery anodes. In this work, super-small metal nanoparticles (2.9 nm in diameter) are *in situ* synthesized and homogeneously embedded in the *in situ* formed nitrogen-doped carbon matrix, as demonstrated by the Si/Ag/C nanohybrid, where epoxy resin monomers are used as solvent and carbon source. With tiny amount of silver (2.59 % by mass), the Si/Ag/C nanohybrid exhibits superior rate performance compared to the bare Si/C sample. Systematic structure characterization and electrochemical performance tests of the Si/Ag/C nanohybrids have been performed. The mechanism for the enhanced rate performance is investigated and elaborated. The temperature dependent *I-V* behavior of the Si/Ag/C nanohybrids with tuned silver contents is measured. Based on the model, it is found that the super-small silver nanoparticles mainly increase charge carrier mobility instead of the charge carrier density in the Si/Ag/C nanohybrids. The evaluation of the total electron transportation length provided

by the silver nanoparticles within the electrode also suggests significantly enhanced charge carrier mobility. The existence of tremendous amounts of super-small silver nanoparticles with excellent mechanical properties also contribute to the slightly improved cyclic stability compared to simple Si/C anodes.

KEYWORDS: silicon; silver nanoparticles; nanohybrid; lithium-ion battery; anode; epoxy resin; super-small

Efficient and durable energy storage devices are essential for volatile and fluctuating renewable energy sources.[1-4] Rechargeable lithium-ion batteries (LIBs) with high power and energy density have attracted significant attention from both industry and academia as a powerful energy storage media. They have been widely used in electric vehicles (EVs), portable electronic devices, and smart grid systems.[5-7] These applications have spurred increasing demand for developing new electrode materials to achieve high energy and/or power density, long cycle life, fast charge rate, and low production cost. Silicon (Si) has emerged as a promising candidate for next-generation LIB anodes due to its unparalleled theoretical capacity compared to commercial graphite (4200 mAh g^{-1} vs. 372 mAh g^{-1}), proper voltage profile, and enhanced operation safety.[8-19] However, the intrinsic drawback of huge volume change during lithiation/delithiation cycles leads to fracture of Si, pulverization of electrodes, and continuous formation/rupture of solid electrolyte interphase (SEI) .[20-23] All of these processes lead to very poor cyclic stability. It has been recognized as one of the most critical neck-points hampering the practical application of the Si-based LIBs anodes.[24] Besides the poor cyclic stability, the rate performance of Si anodes also needs to be improved. [13, 25]Si possesses rather low intrinsic electron conductivity because of its semiconductor nature. Various strategies have been developed to resolve these problems including particle size reduction to the nanoscale level,[20, 26-27] compositing Si with conductive buffer media such as, Cu[28] Ag,[29] and carbonaceous material,[19, 24, 30-33] and constructing hierarchical architectures.[18, 34] Despite of the success of the performance improvement based on the strategies addressed above, the issue of mass loading density of Si has been largely ignored, which is vital for practical applications regarding total energy/power density output.[35-36]

Metal exhibits excellent mechanical property and superior electron conductivity. It has been recognized as one of the most promising buffer media to improve the performance the Si-based anodes.[37-47] Normally quite large amount of metal is needed for surface modification of the silicon.[39, 42-43, 46-47] Nevertheless, excessive incorporation of metal species tends to reduce the overall capacity, increase the cost, and make the coating process complicated and non-feasible. It is essential to develop new strategies to use small amount of metal species, while effectively improve the electrochemical performance of the silicon based anode.[48] Here as a demonstration of our concept, we present the *in situ* synthesis and homogeneous embedding of super-small silver nanoparticles into the silicon/carbon anode. With this strategy, the rate performance is significantly improved and the cyclic stability is slightly enhanced as well. This strategy is in principle universally applicable to other metal system such as copper, and iron. Even though silver has been used previously as a buffer medium to the silicon based anode, the size of the silver particles is large (normally above 20 nm) and decent amount of silver is therefore needed.[43, 46] Here the average size of the as-synthesized silver nanoparticles in this work is significantly reduced to well below 5 nm, which has been rarely used to modify the silicon anode.[29, 49-50] By combing the simultaneous *in situ* synthesis of silver and composition with carbon matrix, it is possible to incorporate the super-small silver nanoparticles into the Si/C composite homogeneously.[51] The super-small size feature and homogeneous dispersion of the silver nanoparticles significantly improve the performance of Si-based anodes with tiny amount of silver.

Recently, a strategy was developed by our group to synthesize TiO_2/C and SiOC/C nanohybrid LIB anodes, where super-small TiO_2 or SiOC nanoparticles were synthesized and homogeneously embedded in a continuous carbon matrix.[52-55] Thermosetting methacrylate monomers were used as

solvent and carbon source. The precursor of TiO_2 (Titanium tetraisopropoxide, TTIP) or SiOC (methacryloxy propyl trimethoxy silane, MPTMS) was dissolved in the resin monomer solution at molecular level. Through photo polymerization, the TTIP or MPTMS was integrated into the methacrylate cross-linking network *via* covalent bonding and/or hydrogen bonding interaction. The calcination process converted the thermosetting polymer into a carbon matrix, while transforming the precursor into TiO_2 or SiOC simultaneously. Because there is almost no melting process for the thermosetting polymer during high temperature calcination, the nucleation, growth, agglomeration, and crystallization of the inorganic nanoparticles were significantly hindered. As a result, super-small TiO_2 or SiOC nanoparticles with very poor crystallinity were *in situ* synthesized and homogeneously embedded in the carbon matrix. Due to the unique structure feature and poor crystallinity of the inorganic particles, unusual electrochemical performance as LIB anodes was observed regarding the TiO_2/C and SiOC/C nanohybrids.[52-55]

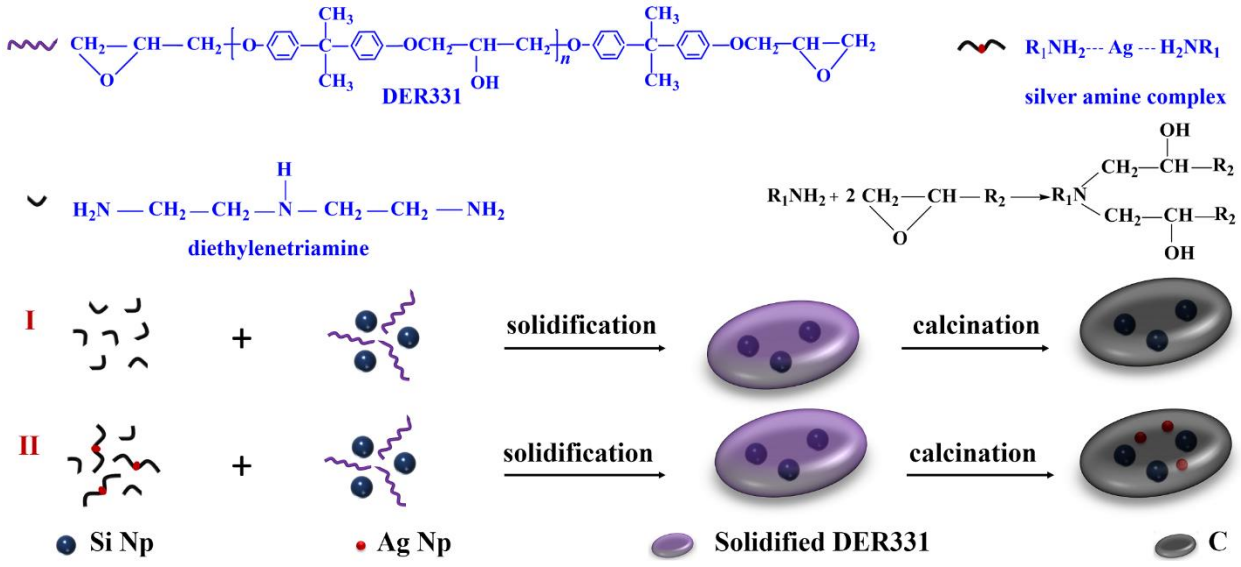

Scheme 1. Schematics of the precursor molecular structure, fabrication process, and structure of the Si/Ag/C nanohybrids. In route I only Si nanoparticles are embedded in the carbon matrix. In route II in addition also silver (Ag) nanoparticles are embedded together with Si nanoparticles.

Inspired by our previous research work, we present an approach to synthesize Si/Ag/C nanohybrid LIB anodes, where super-small silver nanoparticles are *in situ* synthesized and homogeneously embedded in a carbon matrix (**Scheme 1**). Epoxy resin monomers (DER 331) are used as solvent to disperse the Si nanoparticles. The precursor of the silver nanoparticles (silver nitrate) is dissolved in the curing agent of diethylenetriamine (DETA) by forming the coordination bonds between silver and amine function groups. A further hardening process is applied to solidify the liquid epoxy resin solution by mixing the DER 331 resin and DETA solutions. The Si nanoparticles and silver ion species are incorporated into the thermosetting epoxy polymer network. By calcination in argon atmosphere, silver nanoparticles are *in situ* formed. Both silver and Si nanoparticles are homogeneously embedded in to the *in situ* formed continuous carbon matrix.

The strategy addressed in the present study has a few particular advantages as compared to so far published work. Firstly, the formation of the super-small silver nanoparticles is possible because the silver precursor is dissolved in the epoxy resin monomer solution and integrated into the epoxy cross-linking network through strong coordination bonds. The *in situ* carbonization process of the thermosetting epoxy resin network has a rather limited melting process, which effectively inhibits the nucleation and growth of the silver nanoparticles. Secondly, the *in situ* formed silver nanoparticles are homogeneously embedded in the *in situ* formed carbon matrix and the agglomeration of the super-small silver nanoparticles is significantly inhibited. Thirdly, the Ag/C nanohybrid structure helps to retain reasonable powder tap density, which is usually a big challenge for nanostructured materials. Fourthly, continuous carbon matrix is formed instead of the individual carbon shell, which has more capability to accommodate the volume change and absorb mechanical stress of Si.[56] Fifthly, the use of amine based curing agent generates nitrogen doped carbon matrix,

which is good to improve the electron conductivity of the Si/Ag/C nanohybrid, leading to enhanced electrochemical performance. Sixthly, the use of epoxy resin monomer as solvent circumvents the costly, tedious, and environmentally unfriendly post-processing procedure of conventional solvents.

Results and Discussion

The curing degree of the epoxy polymer is evaluated based on the Soxhlet extraction method using acetone as solvent. After extraction, the mass loss values of the Si/DER331 and Si/$AgNO_3$/DER331 composites are about 7.9 % and 2.2 % respectively. The results indicate that the epoxy monomers are almost fully polymerized. Highly cross-linked thermosetting epoxy/silver composites are successfully synthesized.

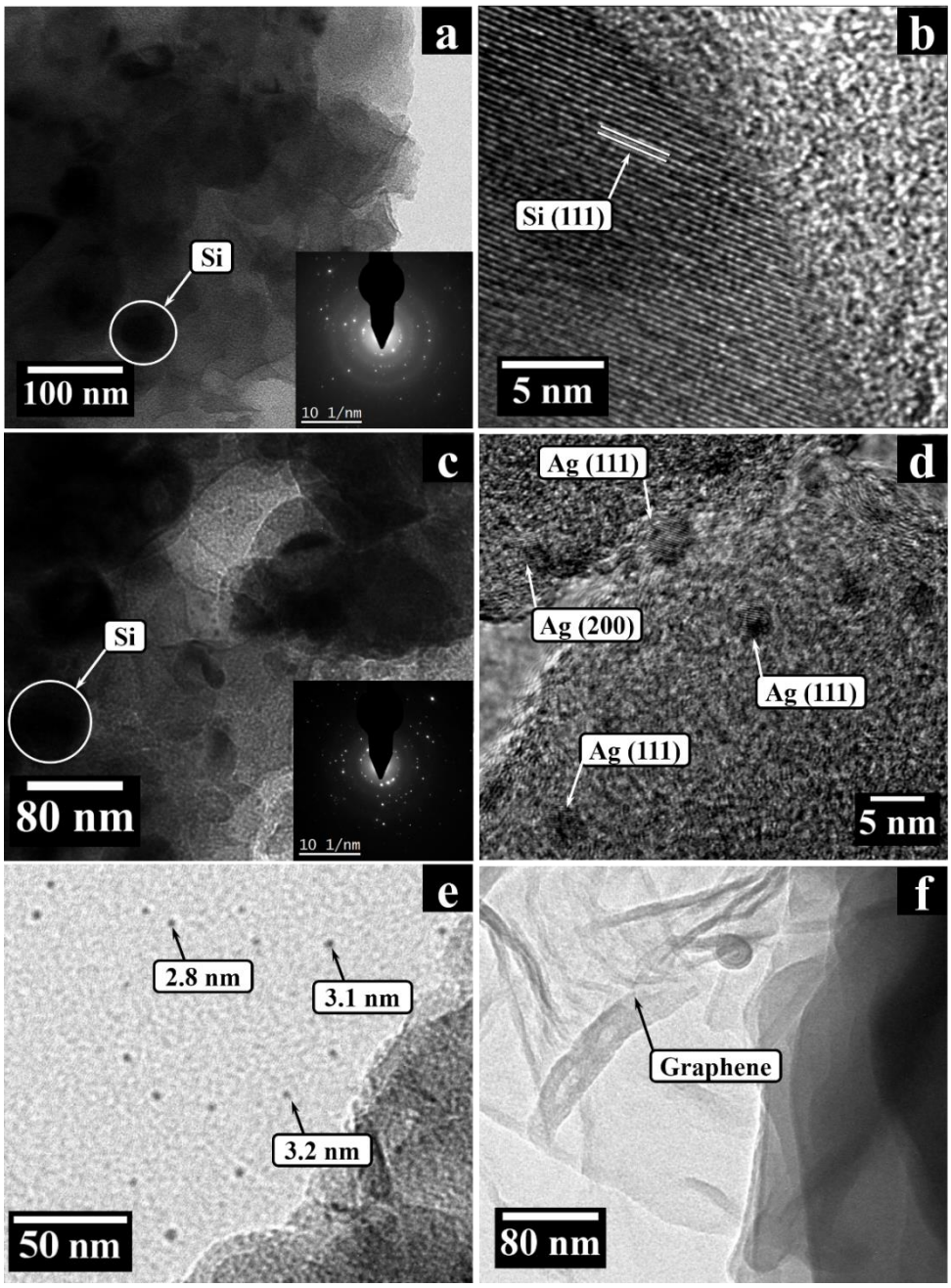

Figure 1. TEM images (a, c), SAED patterns (insets of image a and c), and HRTEM image (b, d) of the Si/C (a, b) and Si/Ag/C nanohybrids (c, d). The silver nanoparticles are embedded in the carbon matrix (e) and the local graphene structure is observed in the Si/Ag/C nanohybrids (f).

The TEM, HRTEM images and SAED patterns of the Si/C nanohybrids are shown in **Figure 1a** and Figure 1b. As shown in Figure 1a, the Si nanoparticles are well embedded in the carbon matrix and have a diameter of around 30 nm. The SAED pattern in Figure 1a and HRTEM image

(Figure 1b) confirm that the Si nanoparticles are well crystallized. Compared to the bare Si/C sample, the Si/Ag/C nanohybrid shows a similar structure feature (Figure 1c), where Si and silver nanoparticles are embedded in carbon matrix. The HRTEM image in Figure 1d indicates that the *in situ* formed silver nanoparticles are of good crystallinity with a size of around 3 nm. Figure 1e displays the structure of the *in situ* formed silver nanoparticles. The average size of the silver nanoparticles is estimated to be 2.9 nm ± 0.5 nm based on the measurement of twelve silver nanoparticles. In addition, a local graphene structure is observed in the Si/Ag/C nanohybrid (Figure 1f). The formation of the graphene structure is due to a catalytic effect of the *in situ* formed silver nanoparticles during carbonization of the epoxy resin[57]. Furthermore, the EDX images show that Si and silver species are homogeneously dispersed in the carbon matrix in both Si/C and Si/Ag/C nanohybrids **(Figure 2)**.

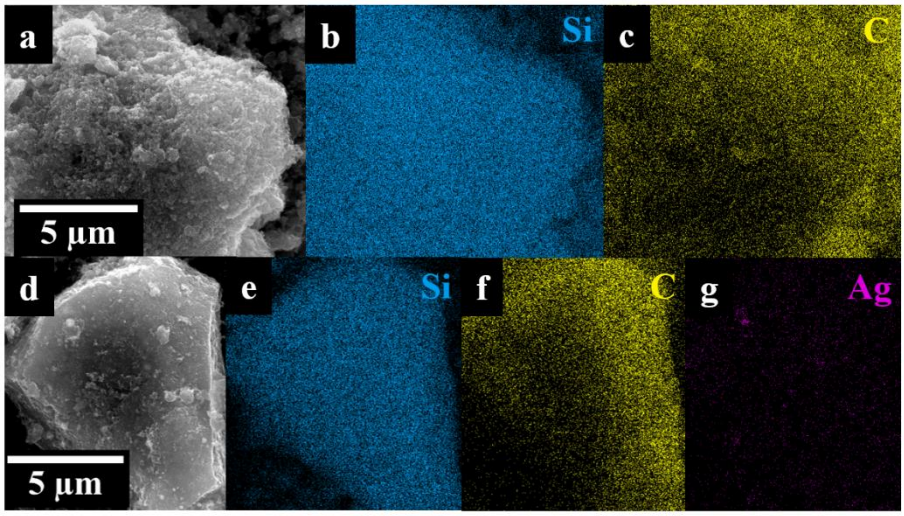

Figure 2. Elemental mapping of the Si/C (a: SEM image, b: element map of Si, c: element map of C) and the Si/Ag/C nanohybrid (d: SEM image, e: element map of Si, f: element map of C, g: element map of Ag).

Figure 3a shows the x-ray diffraction (XRD) patterns of the pristine and calcined nanohybrids.

Before calcination, the Si/DER331 sample exhibits diffraction peaks located at 28.4 °, 47.3 °, 56.1 °, 69.1 °, 76.4 °, and 88.0 °, which are assigned to the (111), (220), (311), (400), (331), and (422) crystal planes of the cubic Si phase (JCPDS NO.27-1402) .[58] Compared to the Si/DER331 sample, the Si/$AgNO_3$/DER331 sample shows weak diffraction peaks of silver metal apart from the peaks belonging to the Si. It indicates that small amount of silver ions are reduced to silver metal during sample preparation due to heat and/or light exposure. After calcination, the Si/C sample exhibits almost identical diffractions peaks to the pristine Si/DER331, which implies that the carbonization process does not modify the crystallinity of the Si nanoparticles. Regarding the Si/Ag/C nanohybrid, besides the peaks originated from the crystalline Si, diffraction peaks with strong intensities belonging to the silver metal are observed. Specifically, the peaks located at 38.1 °, 44.4 °, 64.4 °, 77.4 °, and 81.5 ° are ascribed to the (111), (200), (220), (311) and (222) crystalline planes of the cubic phase of silver (JCPDS card NO. 04-0783) .[38] A broad peak at around 25 ° is found with the calcined samples, which may be presented by the local graphitic carbon structure within the carbon matrix and/or the amorphous SiO_2 formed on the surface of the Si nanoparticles.[59] The broad peak located at around 18 ° is observed only in the polymerized samples resulting from the local crystalline domains in the epoxy resin matrix.

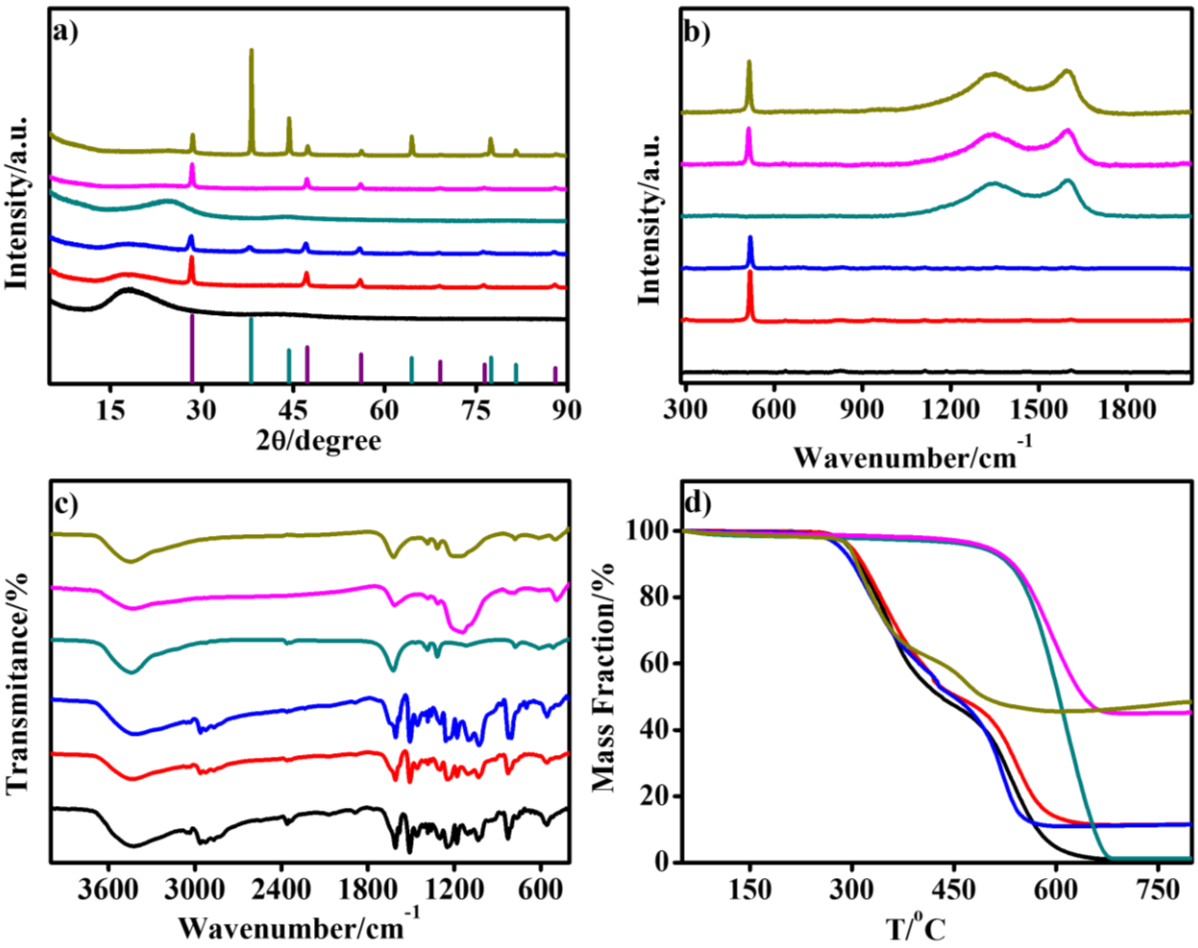

Figure 3. XRD (a), Raman (b), FTIR (c), and TGA (d) of the samples. Black: polymerized DER331; red: Si/DER331; blue: Si/$AgNO_3$/DER331; dark cyan: bare carbon obtained by carbonization of the DER 331 epoxy resin; magenta: Si/C; dark yellow: Si/Ag/C. Purple/dark cyan lines in image 3a are the standard XRD patterns of Si and Ag.

The Raman spectra of the DER331, Si/DER331, Si/$AgNO_3$/DER331, bare carbon, Si/C, and Si/Ag/C are shown in Figure 3b. The peaks at around 515 cm^{-1} originate from the crystalline Si in the Si/DER331, Si/$AgNO_3$/DER331, Si/C, and Si/Ag/C samples. After calcination, two additional peaks located at 1355 cm^{-1} and 1602 cm^{-1} appear in the bare carbon, Si/C and Si/Ag/C samples. The two peaks correspond to the A_{1g} mode of the disordered carbon (D band) and E_{2g} mode of the graphitic carbon respectively (G band). The integrated intensity ratios of the D band over the G

band are 3.14 (Si/C) and 3.26 (Si/Ag/C). It means that the disordered carbon is a major component within the carbon matrix. Furthermore, the increased disordered carbon content in the Si/Ag/C nanohybrid suggests that the addition of silver ions enhances the cross-linking degree of the epoxy polymers, leading to increased char yield from the aliphatic polymeric structural units.

Figure 3c shows the FTIR spectra of the samples including DER331, Si/DER331, Si/$AgNO_3$/DER331, bare carbon, Si/C, and Si/Ag/C. Concerning the samples before calcination, no peaks corresponding to the cyclic epoxy functional group is observed with the DER331, Si/DER331, and Si/$AgNO_3$/DER331 samples. The results indicate that the epoxy groups are completely cross-linked induced by the DETA curing agent. Regarding the calcined samples, a characteristic peak at 1620 cm^{-1} derived from the conjugation bond C=N are observed in the bare carbon, Si/C, and Si/Ag/C samples. Particularly, the characteristic peaks at around 1100 cm^{-1}, 800 cm^{-1} and 480 cm^{-1} in the Si/C and Si/Ag/C samples can be assigned to SiO_2 due to partial surface oxidation of the Si nanoparticles.[60] The FTIR results indicate that nitrogen-doped carbon is obtained after carbonization due to the presence of the DETA curing agent. By comparing the FTIR profiles of the samples before and after calcination, it is found that the number of the peaks within the long wavelength range is significantly reduced after calcination. It reflects the fact that most of the organic moieties of the polymers are burned away. The broad peak located at 3425 cm^{-1} refers to the stretching vibration of the N-H bond in amine. The existence of the N-H bond in the polymerized samples indicates only part of the reactive hydrogen atoms is used for the cross-linking reaction. In addition, the existence of the broad peak after calcination indicates the nitrogen atoms are not fully removed during calcination. The overlapped peaks at 2870 cm^{-1} and 2960 cm^{-1} refer to the symmetric bending vibration and antisymmetric vibration of the C-H bond in the methyl group

of the pristine samples. The peak disappears after calcination, which indicates that the methyl group is completely burned off.

Figure 3d shows the TG curves of the pristine and calcined samples measured in air atmosphere. The polymerized samples start to decompose from around 300 °C evidenced by the mass loss. Further mass loss at around 500 ℃ in the samples of DER331, Si/DER331, Si/$AgNO_3$/DER331, bare carbon and Si/C originates from the burning of the carbon. Compared with the Si/C and bare carbon samples，the early mass loss at around 300 ℃ in the Si/Ag/C nanohybrid is due to the presence of the graphene, which promotes the burning process by enhanced heat and gas transportation.[57] The measured residual mass at 720 °C of the Si/C nanohybrid is about 42 wt%, which corresponds to the Si content. For the Si/Ag/C nanohybrid, the remaining mass of 46 wt% at 650 °C is ascribed to the total amount of Si and Ag_2O. The silver content in Si/Ag/C nanohybrid obtained from the ICP-OES experiment is 2.59 wt%. The exact content of Si in Si/Ag/C can be deduced from the results of TG and ICP-OES test. As a result, 43.3 wt% of Si are included in the Si/Ag/C nanohybrid.

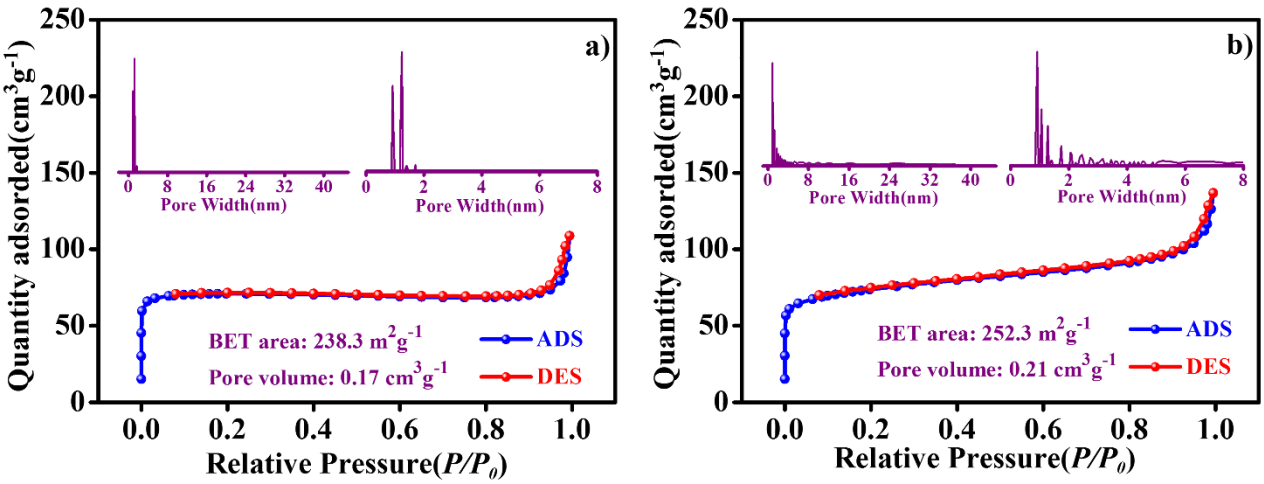

Figure 4. N_2 adsorption/desorption isotherm curves and corresponding pore size distribution

profiles (insets) of the Si/C (a) and Si/Ag/C (b) nanohybrids. ADS: adsorption, DES: desorption.

Brunauer-Emmett-Teller (BET) gas sorption measurements are performed to investigate the porosity of the Si/C and Si/Ag/C nanohybrids. N_2 adsorption-desorption isotherms are shown in **Figure 4**, where corresponding porosity distribution profiles derived by density functional theory are depicted in the insets. As shown in the adsorption-desorption isotherms in Figure 4a and Figure 4b, the Si/C and Si/Ag/C nanohybrids exhibit a mixed characteristics of micropores and mesopores. The rapid growth at low pressure can be assigned to the filling of the micropores, and the existence of the small hysteresis loop at high pressure results from the filling of the mesopores[61]. However, it can be found that the hysteresis loop is quite small, which suggests the presence of mesopores is very limited in the carbon matrix. The pore size distribution profiles of the Si/C show that micropores exist with a quite uniform bimodal size of 0.9 nm and 1.2 nm. Regarding the Si/Ag/C nanohybrid, the pore size distribution is slightly broader than that of the Si/C sample. While micropores with the size in the range of from 0.8 nm to 1.8 nm are observed, small amount of mesopores are also exhibited in the profile. The relative broad size distribution of the pores is due to the presence of additional local graphene structure and the heterogeneous interface between the carbon matrix and silver nanoparticles. The BET specific surface area of the Si/C and Si/Ag/C nanohybrids are measured to be 238.3 m^2g^{-1} and 252.3 m^2g^{-1} respectively. And the total pore volume of the Si/C and Si/Ag/C are 0.17 cm^3g^{-1} and 0.21 cm^3g^{-1} respectively ($P/P_{0:}$ 0.9942). The slightly increased specific surface area and pore volume of the Si/Ag/C nanohybrid are likely due to the formation of local graphene structure and the incorporation of super-small silver nanoparticles.

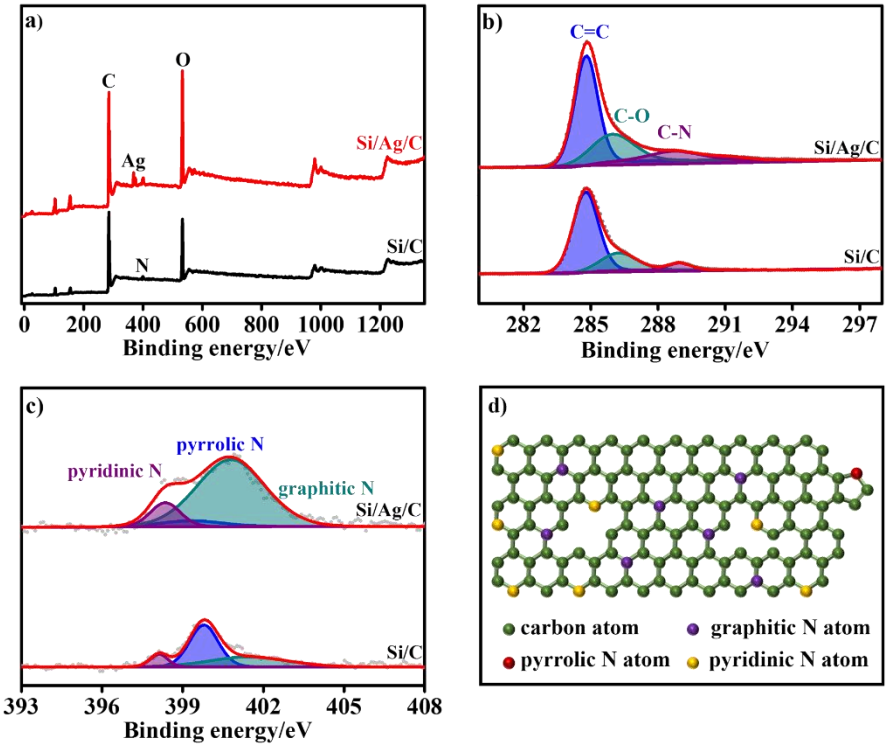

Figure 5. XPS spectra of the Si/C and Si/Ag/C nanohybrids: survey spectrum of the Si/C and Si/Ag/C (a), High resolution XPS spectra of the C1s in the Si/C and Si/Ag/C (b), high resolution XPS spectra of the N1s in the Si/C and Si/Ag/C (c), and schematic structure of nitrogen doped carbon (d). Grey point: experimental data, red line: fitted curves.

The x-ray photoelectron spectra (XPS) of the Si/C and Si/Ag/C samples suggest that Nitrogen doping happens in the carbon matrix because the amine based curing agent (DETA) is used (**Figure 5**). The characteristic peaks at 285 eV, 400 eV and 532 eV in Figure 5a correspond to the C1s, N1s and O1s, respectively[62]. As exhibited by Figure 5b, the C1s spectrum of the Si/C and Si/Ag/C nanohybrids can be deconvoluted into three individual peaks. The sharp peak at 284.5 eV corresponds to the sp^2 carbon atoms, which indicates the presence of graphitic carbon. The characteristic peak at 286.2 eV refers to the C-O bonding. And the peak at 289 eV is ascribed to the C-N bond, which originates from the incorporation of the diethylenetriamine curing agent in the

epoxy polymer network.[63] It is found that the intensity of the peak at 286.2 eV is much weaker than that of the peak at 284.5 eV. It indicates the existence of only small amount of C-O bonding within the carbon matrix.[64] Furthermore, compared with the Si/C sample, the full width of half-maximum (FWHM) of the peak at 289 eV in the Si/Ag/C nanohybrid is slightly increased. It means that the incorporation of silver facilitates the formation of the C-N bond. The detailed XPS spectra of N1s further proves the existence of the nitrogen species in the samples (Figure 5c). The characteristic peaks at 398.2 eV, 399.5 eV and 401.2 eV confirm the existence of pyridinic N, pyrrolic N and graphitic N (Figure 5d) in the carbon matrix of the Si/C and Si/Ag/C nanohybrids. It seems that the relative compositions of the graphitic N and pyrrolic N are increased significantly compared to the pyridine N in the Si/Ag/C nanohybrid.

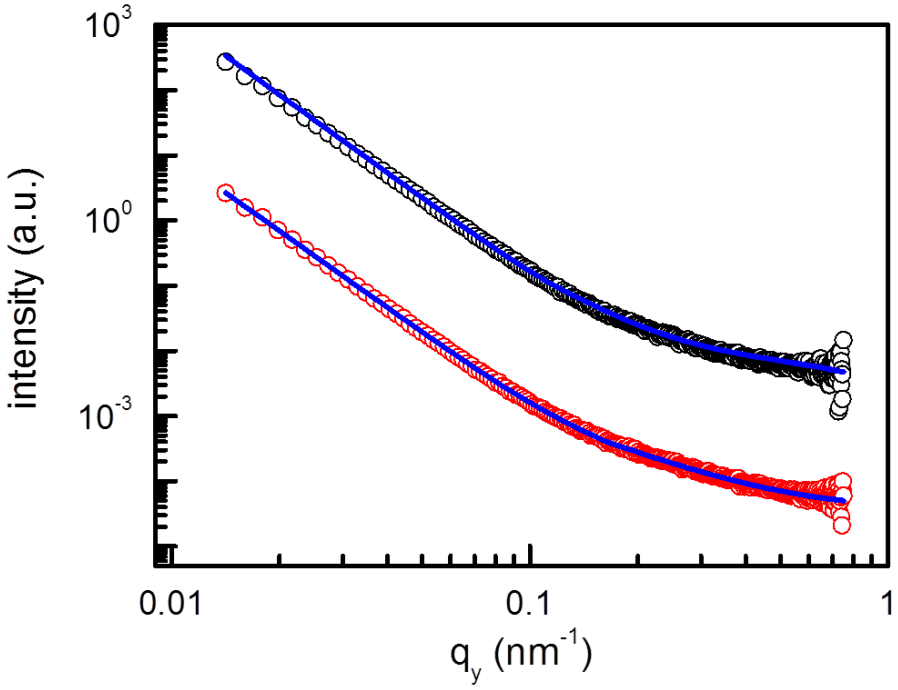

Figure 6. Experimental (open circle) and fitting (solid lines) SAXS of the Si/C (black circle) and Si/Ag/C (red circle) nanohybrids.

Besides the imaging analysis in local areas, the average statistic structure information on the

Si/C and Si/Ag/C nanohybrids is investigated by SAXS. According to **Figure 6**, similar scattering behaviors are observed in the SAXS data, in which both curves are displayed with no distinguished peaks. This reveals random distribution of nanoparticles. Being confirmed by TEM, spherical Si and Ag nanoparticles are dispersed randomly inside carbon matrix. Therefore, the SAXS cuts are modeled with only sphere form factor with a Gaussian distribution function. No structure factor is applied to the fitting. According to the fitting, Si particles with diameter of 42 ± 4 nm are obtained in the Ag-free sample. With incorporation of silver, the size of Si particles stays as a constant, and 3 ± 1 nm of silver nanoparticles are present in the nanohybrids.

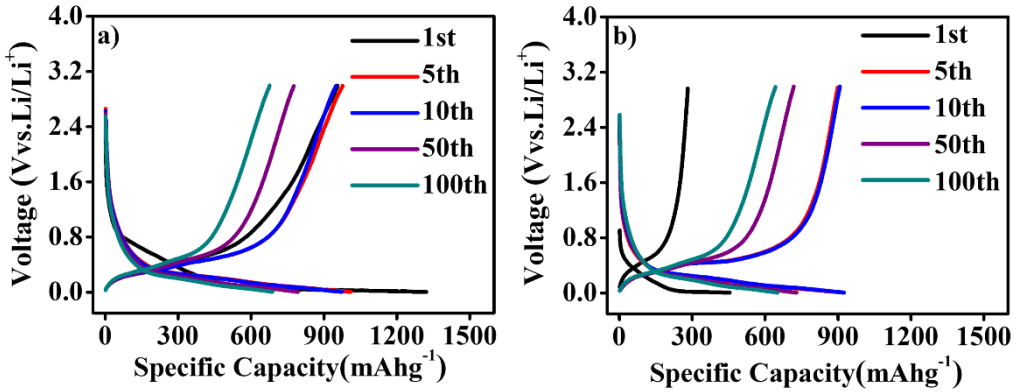

Figure 7. Discharge/charge curves (0.2 C, 1C = 1000 mAg^{-1}) of the Si/C (a) and Si/Ag/C nanohybrids (b).

The discharge and charge curves of the Si/C and Si/Ag/C nanohybrids are shown in **Figure 7** for a current density of 200 mAg^{-1} between 0.005 V and 3 V (vs. Li/Li^+). It is reported that the crystalline Si possesses a well-defined discharging plateau at about 0.1 V and a charging potential at about 0.45 V during the lithiation/delithiation processes.[65] And the pyrolyzed carbon material obtained from the polymer resin often exhibits unobvious plateau during the discharge/charge processes.[52] Therefore, the Si/C and Si/Ag/C nanohybrids synthesized in this work exhibit a mixed behavior of Si and pyrolytic carbon. Compared with the discharge/charge curves of the Si/C

composite, no additional characteristic plateau can be found in the Si/Ag/C nanohybrids, which suggests that the lithiation of silver is rather limited. Correspondingly, it is reasonable to conclude that the capacity mainly comes from the Si and carbon matrix.[66] Furthermore, the discharging plateau at around 0.6 V in the first cycle is assigned to the formation of the SEI films.[67] It is also found that the Si/Ag/C composite undergoes an activation process in the first few cycles, which may result from the gradual infiltration of the electrolyte.[68] The 5th and 10th charge/discharge curves of the Si/C and Si/Ag/C nanohybrids are almost identical, which indicates that the electrodes possess good cyclic stability until at least the 10th cycle. Regarding the discharge/charge profiles of the 50th and 100th cycle of the Si/C and Si/Ag/C electrodes, the patterns are still quite similar to the curves of the 10th cycle. It means that the fundamental electrochemical process is stable even though some capacities are lost with increased cycles.

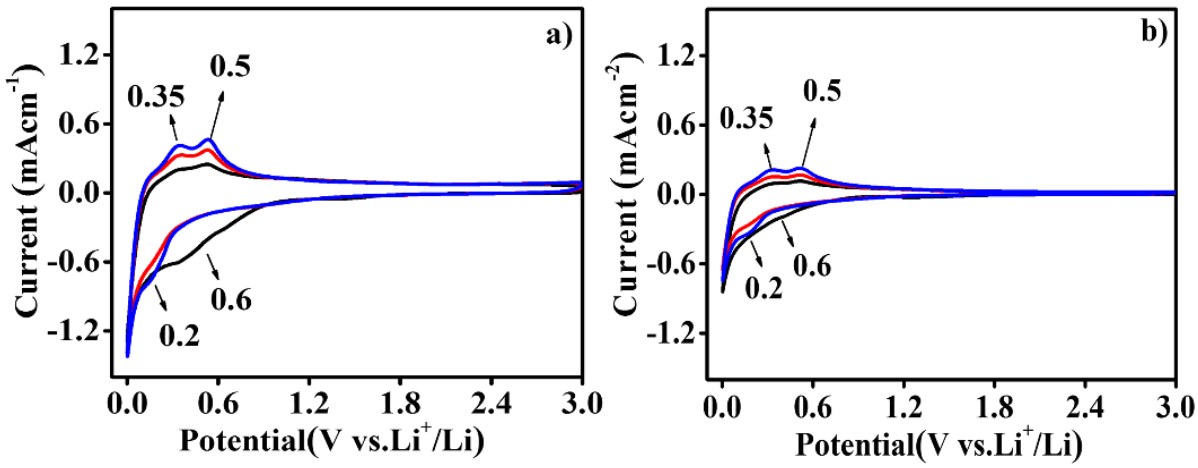

Figure 8. Cyclic voltammetry (CV) of the Si/C (a) and the Si/Ag/C (b) electrodes with different cycles. (black: 1st, red: 2nd, and blue: 3rd).

Figure 8 shows the cyclic voltammetry (CV) of the Si/C and the Si/Ag/C electrodes. The broad cathodic peak at around 0.6 V is observed in the first cycle and then disappears in the subsequent cycles (**Figure 8a**, **8b**). It indicates the formation of a SEI film on the surface of the active material,

which is in good agreement with the discharge/charge curves[67]. Considering that the characteristic peak around 0.6 V mainly appears in the carbon based electrode material, it suggests that the Si nanoparticles are well embedded in the carbon matrix. The anodic peaks at 0.35 V and 0.5 V are associated with the successive transitions from highly lithiated Si to less-lithiated and further non-lithiated Si.[69-70] A new peak is observed at 0.2 V as opposed to the first discharge process, resulting from the reaction of lithium with Si to form amorphous Li_xSi, which needs a possible activation process during the insertion/extraction.[51, 71-73] Peaks related to the reaction between Ag and Li are not detected, which indicates that the lithiation of silver is quite limited.[65]

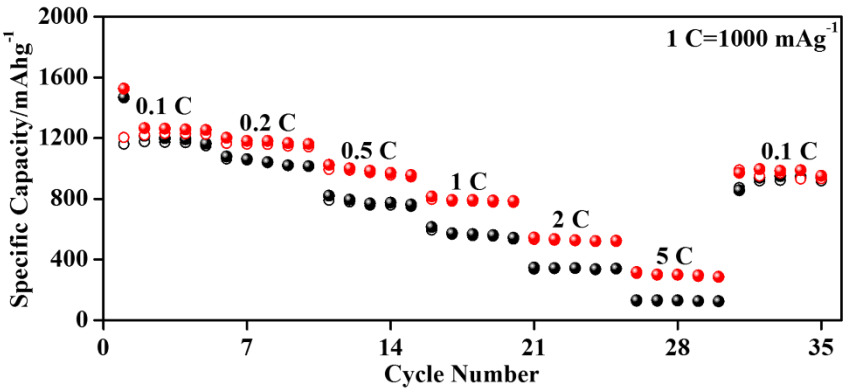

Figure 9. Rate performance of the Si/C and Si/Ag/C nanohybrids. Black: Si/C, red: Si/Ag/C, sphere: discharge capacity, open circle: charge capacity.

The rate performance of the Si/C and Si/Ag/C nanohybrids at different current densities is shown in **Figure 9**. And the corresponding average discharge capacities of the Si/C and Si/Ag/C nanohybrid electrodes at different current densities are listed in **Table 3**.

Table 3. Average discharge capacities of the Si/C and Si/Ag/C summarized from Figure 9.

Sample	Average discharge capacities at different current densities/mAhg^{-1}						
	0.1 C	**0.2 C**	**0.5 C**	**1 C**	**2 C**	**5 C**	**0.1 C**
Si/C	1247	1043	784	572	342	128	926
Si/Ag/C	1313	1179	988	795	530	299	978

Note: 1 C = 1000 mAg^{-1}.

Compared to Si/C, the Si/Ag/C nanohybrid exhibits higher capacity at each individual current density, especially at the high current densities. For example, the Si/C electrode shows average discharge capacities of 784 $mAhg^{-1}$, 572 $mAhg^{-1}$, 342 $mAhg^{-1}$ and 128 $mAhg^{-1}$ at 0.5 C, 1 C, 2 C and 5 C respectively. However, the Si/Ag/C nanohybrid electrode exhibits average discharge capacities of 988 $mAhg^{-1}$, 795 $mAhg^{-1}$, 530 $mAhg^{-1}$, and 299 $mAhg^{-1}$ at the same current densities (Table 3). When the current density is changed back from 5 C to 0.1 C, the average discharge capacities of the Si/C and Si/Ag/C electrodes are restored to 926 $mAhg^{-1}$ and 978 $mAhg^{-1}$ respectively. The results suggest that the Si/Ag/C possesses good cyclic stability and rate performance. The significantly improved rate performance of the Si/Ag/C composite mainly benefit from the uniform dispersion of super-small silver nanoparticles in the carbon matrix. The incorporation of the silver nanoparticles leads to a significant increase of the electron transportation path within the nanohybrid.[74]

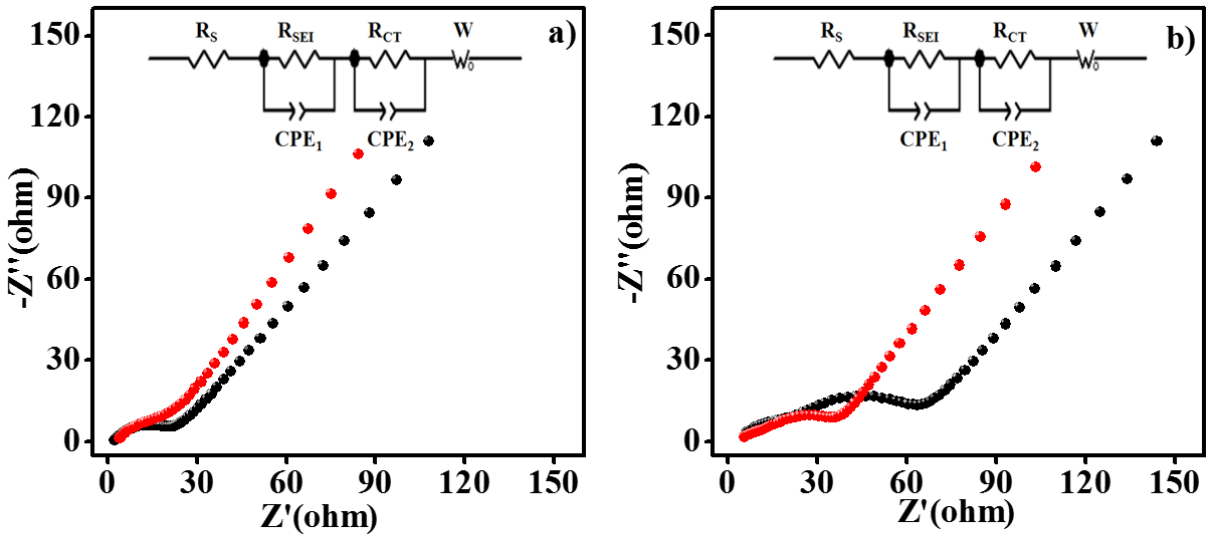

Figure 10. Electrochemical impedance spectra of the Si/C (black) and the Si/Ag/C (red) nanohybrid electrodes after 3 cycles (a) and after 100 cycles (b).

Table 5. Representative fitting data of EIS spectroscopy of the Si/C and Si/Ag/C nanohybrids.

R / SAMPLE	Si/C	Si/Ag/C
$(R_S+R_{SEI}+R_{CT})_3$ (Ω)	25.4	20.3
$(R_S+R_{SEI}+R_{CT})_{100}$ (Ω)	65.6	33.2

Figure 10 shows the electrochemical impedance spectra of the Si/C and Si/Ag/C nanohybrids after 3 cycles and 100 cycles respectively. The insets in the spectrum refer to the equivalent circuit model used to fit the EIS experimental profiles.[75] Although the slopes of the straight lines are very similar, the dimensions of the semicircles are different with the incorporation of the silver nanoparticles. Compared to the impedance spectrum of the Si/C and Si/Ag/C after three cycles, the semicircle dimensions of the Si/C and Si/Ag/C after 100 cycles are obviously increased. It suggests that the charge transfer resistance of electrodes is increased along with increased cycles, which is due to the partial degradation of the electrode structure.[75] In addition, the semicircle dimensions of the Si/Ag/C nanohybrids after three and one hundred cycles are significantly narrower compared to those of the Si/C electrodes with the same cycle. This finding is also supported by the fitted parameters listed in **Table 5**. The decreased resistance values in the Si/Ag/C nanohybrids originate from the homogeneous incorporation of the super-small silver nanoparticles in the carbon matrix. The silver metal has superior electron conductivity than the carbon matrix. Additionally, the super-small structure feature of the silver nanoparticles is particularly helpful to improve the overall electron transportation property of the nanohybrids. The silver nanoparticles provide tremendous amounts of additional charge carrier transport routes with exceptional electron conductivity in the carbon matrix, which effectively increases the charge carrier transfer resistance. The increase of the charge carrier transportation brought by the silver nanoparticles is calculated as following:

Radius of original particle: R_1

The particle with the radius of R_1 is divided into N particles with the radius of R_2.

Number of the new particles: $\mathrm{N} = \left(\frac{\mathrm{R}_1}{\mathrm{R}_2}\right)^3$

Total surface area incease: $\frac{A2}{A1} = N * \frac{4\pi {\mathrm{R}_2}^2}{4\pi {\mathrm{R}_1}^2} = \left(\frac{\mathrm{R}_1}{\mathrm{R}_2}\right)^3 * \frac{4\pi {\mathrm{R}_2}^2}{4\pi {\mathrm{R}_1}^2} = \frac{\mathrm{R}_1}{\mathrm{R}_2}$

Total charge carrier transportation length incease: $\frac{L2}{L1} = \mathrm{N} * \frac{2\mathrm{R}_2}{2\mathrm{R}_1} = \left(\frac{\mathrm{R}_1}{\mathrm{R}_2}\right)^3 * \frac{\mathrm{R}_2}{\mathrm{R}_1} = \left(\frac{R1}{R2}\right)^2$

It can be found that the super-small silver nanoparticles provide extra transport routs by a factor of $(R_1/R_2)^2$. Furthermore, it is interesting to observe that the charge carrier transportation length enhancement is even more pronounced than that of the surface area, which is only proportional to the order of R_1/R_2. Considering that there is 2.59 wt% of silver with the average diameter of 2.9 nm in the Si/Ag/C nanohybrid electrode with the mass loading density of 1.21 $mgcm^{-2}$, the total charge carrier transport length provided by the silver nanoparticles on the copper current collector is derived as following:

$1.21 \times 10^{-3} gcm^{-2} \times 2.59\ \% \div (10.49 gcm^{-3}) \div \left(\frac{4}{3} \times \pi \times (1.45 \times 10^{-7} cm)^3\right) \times 2.9 \times 10^{-9} m = 6.7 \times 10^5 mcm^{-2}$

It can be found that the silver nanoparticles bring a total length of 6.7×10^5 m for electron transportation on each 1 cm^{-2} electrode. It is reasonable to ascribe the significantly improved rate performance of the Si/Ag/C nanohybrid anode to the existence of the super-small silver nanoparticles.

Besides the evaluation of the charge carrier transportation length provided by the super-small silver nanoparticles, the mechanism of charge carrier transportation of the Si/Ag/C nanohybrids is also investigated. The temperature dependent electron conductivity of the Si/Ag/C nanohybrids with the silver mass composition of 0, 2.591 %, 3.994 %, and 4.552 % are measured. The carbon matrix mainly consists of graphite crystalline and amorphous carbon as confirmed by Raman and TEM

measurements. Graphite is a semimetal with delocalized carriers, whereas amorphous carbon is a disordered system where transportation relies on hopping between discrete energy levels. The high conductivity and the ohmic character displayed in **Figure 11a** and **Figure S1** in the supporting information implies that the dominant transportation mechanism in the Si/Ag/C nanohybrid is band-like rather than hopping between desecrate sites. The resistivity decreases monotonically with the increasing temperature, indicative of a semiconductor-behavior. We hereby model the Si/Ag/C system as a semiconductor system where the transportation is determined by the density and the mobility of the charge carriers. The charge carrier density depends on the thermal population of the band edge of the graphite whereas the carrier mobility counts both the carrier scattering within the graphite flakes and their transportation between the flakes through the amorphous carbon regions. Assuming identical mobility of electrons and holes, the resistivity reads[76]

$$\rho = \left(q\mu n\right)^{-1} \quad (1)$$

where q is the elementary charge, n is the density of carriers including electrons and holes, and μ is the mobility of the carriers.

We note that the carrier mobility, μ, has been assumed to take the form of

$$\mu = \mu_i^{-1} + A_0 T \quad (2)$$

in modeling the temperature dependent conductivity of graphite thin flakes,[76] where μ_i^{-1} is the contribution from static scattering centers and A_0 is a constant corresponding to the electron-phonon scattering in graphite. In this hybrid Si/Ag/C system, A_0 can be seen as the first-order temperature coefficient with the scattering and the thermal activation incorporated.

For simplicity, holes and electrons are treated equally, which yields a carrier density, n, as

$$n = 2\int_0^{+\infty} f(E)N(E)\mathrm{d}E \quad (3)$$

where $f(E)$ is the Fermi-Dirac distribution function, and $N(E)$ is the density of states (DOS) for 2D electrons in the graphite. As the thermally excited carriers populate only the conduction band minimum and valance band maximum, the simple two-band (STB) model with parabolic band edge can well describe the energy spectrum,[77] which reads

$$E(k) = k^2/2m^* \quad (4)$$

where m^* is the band effective mass of electrons and holes and k is the wave vector in vicinity of the band edge. By taking the two-dimensional DOS and substituting Eqs. (2, 3) into Eq. (1), we get

$$\rho(T) = (A + BT)\cdot\left[T\ln\left(1 + e^{E_F/k_BT}\right)\right]^{-1} \quad (5)$$

where A and B are fitting parameters with the coefficients in Eq. (2) and the integral constant of Eq. (3) absorbed, E_F is the Fermi level, and k_B is the Boltzmann constant.

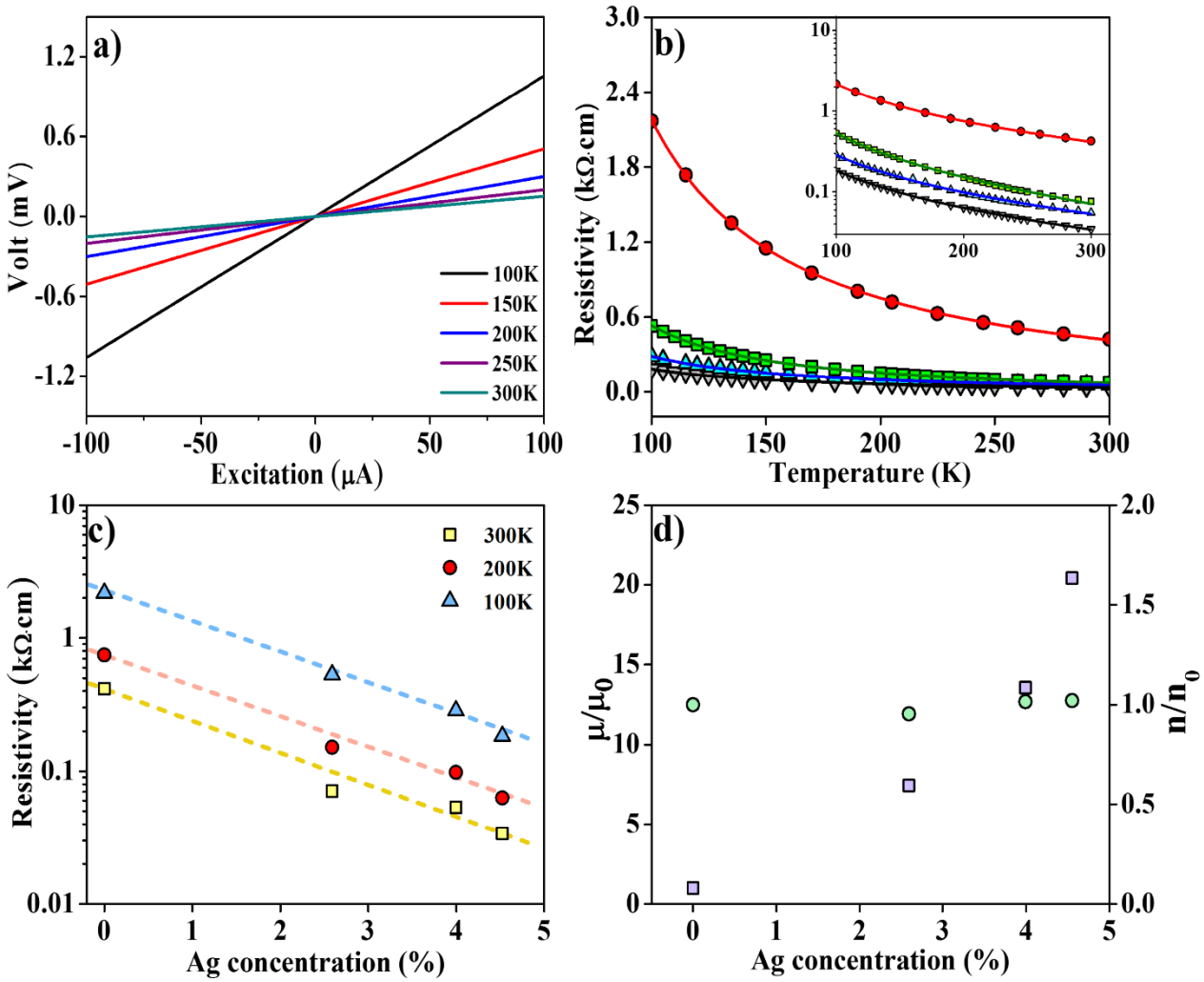

Figure 11. Typical I-V curves of the Si/Ag/C nanohybrid with the silver composition of 4.552 % at different temperatures (a), temperature dependent resistivity profiles of the Si/Ag/C nanohybrids (b) (silver content: 0 % (red), 2.591 % (green), 3.994 % (blue), and 4.552 % (gray), symbols: experimental data, lines: fitting results), resistivity-silver content correlation of the Si/Ag/C nanohybrids with varied silver contents at different temperatures (c, symbols: experimental data, dash lines: guide to eyes), mobility (purple square) and charge carrier density (green circle) of the Si/Ag/C nanohybrids with different silver compositions.

In the Si/Ag/C system, the low concentration of Ag particles unlikely form percolating networks; the temperature dependence of the ρ-*T* correlation for all the Ag concentrations exhibited

in Figure 11b confirms that the Si/Ag/C system is semiconductor-like, indicating that the charge transportation is mainly in the carbon matrix. Therefore Eq. (5) still applies. Using Eq. (5), the temperature dependence of the resistivity for the Si/Ag/C system with different concentrations of Ag nanoparticles can be well fitted, as show in Figure 11b. The fitting parameters, *A*, *B* and the Fermi level E_F are listed in **Table 6**. With increasing concentration of Ag nanoparticles, the resistivity decreases, as presented in Figure 11c. The room-temperature mobility and carrier density for different Ag concentrations, normalized by their values at zero Ag concentration, are plotted in Figure 11d. It is clearly seen that the mobility is significantly enhanced with increasing Ag concentration, whereas the carrier density is insensitive to the Ag concentration. This implies that the improvement of the conductivity by incorporating Ag nanoparticles is not due to the field effect as in the cases of the metallic ion intercalated systems. Here the mechanism is proposed as follows. In the Si/Ag/C system, there is an accumulation of charge carriers in the amorphous carbon regions between the graphite flakes because of the imbalance between the band-like transportation in the graphite flakes and the hopping transportation in the amorphous carbon regions. These accumulated charges act as scattering centers *via* long-range Coulomb interaction to the carriers in the graphite flakes, and therefore lower the carrier mobility for the whole system. The Ag nanoparticles embedded into the amorphous carbon regions provide extra pathways for the accumulated charges by shortening their hopping distance. As a consequence, the Si/Ag/C system has an improved transportation behavior due to the reduced scatterings among the charge carriers.

Table 6. Fitting results of the Si/Ag/C nanohybrids with different silver concentrations.

Ag %	***A*** **(kΩ·cm·K)**	***B*** **(Ω·cm)**	E_F **(meV)**
0	190.4	-149.6	-6.0

2.591	21.7	-33.0	-7.6
3.994	13.4	-13.2	-5.5
4.552	8.8	-9.1	-5.3

It is worth noticing that the resistivity of the whole system decreases exponentially within the regime of low Ag concentration as suggested by Figure 11c. It indicates a significant improvement to the system's conduction by embedding the silver nanoparticles into the carbon matrix. We therefore argue that the incorporation of tiny amount of the *in situ* formed super-small silver nanoparticles essentially enhances the charge transportation in the amorphous carbon regions.

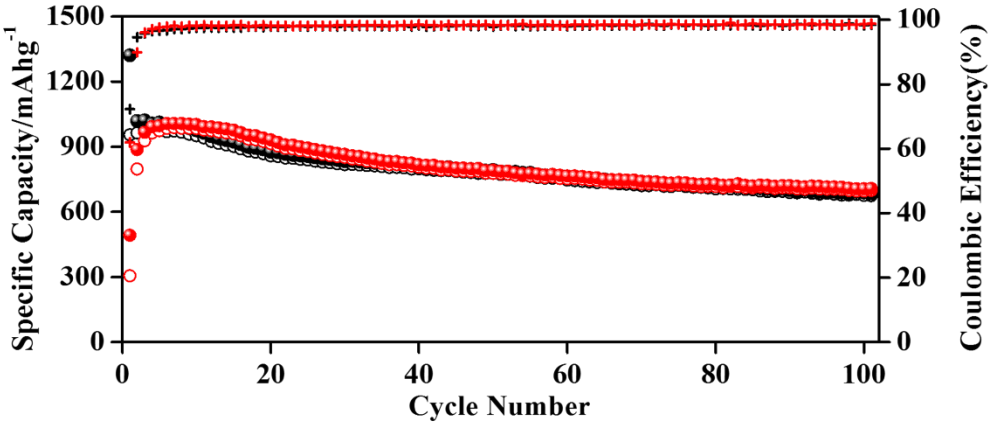

Figure 12. Cyclic performance of the Si/C and Si/Ag/C nanohybrids. Black sphere/black open circle: discharge/charge capacity of Si/C, red sphere/red open circle: discharge/charge capacity of Si/Ag/C. black cross: coulombic efficiency of Si/C, red cross: coulombic efficiency of Si/Ag/C.

The cyclic stability test is performed at a current density of 0.2 C (1 C = 1000 mAg^{-1}) with the voltage window between 0.005 V and 3.0 V (vs. Li/Li^+). **Figure 12** and **Table 7** compare the cyclic performance of the Si/C and Si/Ag/C nanohybrids. The capacity retention is calculated by dividing the capacity of the 100^{th} cycle with the maximum charge capacity. And the average capacity decay rate is calculated based on the expression of (1-capacity retention)/100. It is found that the incorporation of the silver nanoparticles slightly improves the cyclic stability. As detailed in Table 7,

the initial coulombic efficiency values of the Si/C and Si/Ag/C nanohybrids are 72.3 % and 61.9 % respectively. The slightly decreased initial coulombic efficiency of the Si/Ag/C nanohybrid is likely due to increased specific surface area. Furthermore, the maximum charge capacity of the Si/C and Si/Ag/C nanohybrids are 977 $mAhg^{-1}$ and 988 $mAhg^{-1}$ respectively. And the charge capacity of the Si/C and Si/Ag/C nanohybrids at the 100^{th} cycle are 674 $mAhg^{-1}$ and 699 $mAhg^{-1}$. Therefore, the capacity retention values of the Si/C and Si/Ag/C electrode after 100 cycles reach 69 % and 71 % respectively corresponding to an average capacity decay rate of 0.31 % and 0.29 %. The good cyclic stability of the Si/C and Si/Ag/C nanohybrids results from the homogeneous embedment of the Si nanoparticles in the *in situ* formed continuous carbon matrix.[55] The slightly improved cyclic stability of the Si/Ag/C compared to the Si/C sample may also originate from the presence of the silver nanoparticles. The silver nanoparticles possess excellent mechanical properties and tremendous amounts of super-small silver nanoparticles exist in the Si/Ag/C nanohybrid. The silver nanoparticles can act as stress absorption center to stabilize the electrode upon huge volume change.

Table 7. Cyclic performance details of the Si/C and Si/Ag/C depicted in Figure 11.

Sample	Initial coulombic efficiency	Maximum charge capacity	Charge capacity of the 100^{th} cycle	Capacity retention	Average capacity decay rate (%)
Si/C	72.3 %	977 $mAhg^{-1}$	674 $mAhg^{-1}$	69 %	0.31 %
Si/Ag/C	61.9 %	988 $mAhg^{-1}$	699 $mAhg^{-1}$	71 %	0.29 %

The SEM and optical microscopy images in **Figure 13** depict the structure change of the Si/C and Si/Ag/C nanohybrid electrodes before and after cycling test. Figure 13a shows a piece of Si/C fragment with the size of around 2 μm on the surface of the current collector. The low magnification SEM image shows that the surface of the electrode is full of micrometer-sized aggregates (Figure 13a′), which is consistent with the Figure 13a. Compared to the SEM images,

the optical image in Figure 13a″ shows that the electrode is quite homogeneous and smooth at macroscopic scale. The structures of the Si/C electrode after cycling are depicted in the SEM images of Figure 13b, 13b′, and optical image of Figure 13b″. Some voids are observed on the surface of the electrode (Figure 13b), which may reflect the porous structure within the electrode. The existence of the pores may be due to the volume expansion of the Si nanoparticles. Compared to the electrode before cycling test, the cycled Si/C electrode possesses more serious fragmentation as shown in Figure 13b′. It indicates that the pulverization process happens caused by continuous volume change of the Si nanoparticles. Despite of the obvious structure change revealed by the SEM images, the optical image in Figure 13b″ still shows homogeneous smooth surface. It indicates that the electrode still retains good structure integrity after cycles.

Figure 13c and Figure 13c′ show the morphology of the Si/Ag/C electrode before cycling. The images exhibit similar structures compared to the Si/C electrode. The optical image of the Si/Ag/C also confirms that the electrode has excellent electrode integrity (Figure 13c″). Compared with the SEM images of the Si/C electrode after cycling, no voids are observed (Figure 13d). Figure 13d′ and Figure 13d″ exhibit similar structure with the Si/C electrode. It indicates that similar process takes place in the Si/Ag/C electrode along with increased cycles compared to the Si/C electrode. This could be the reason why both Si/C and Si/Ag/C electrodes exhibit similar cyclic performance.

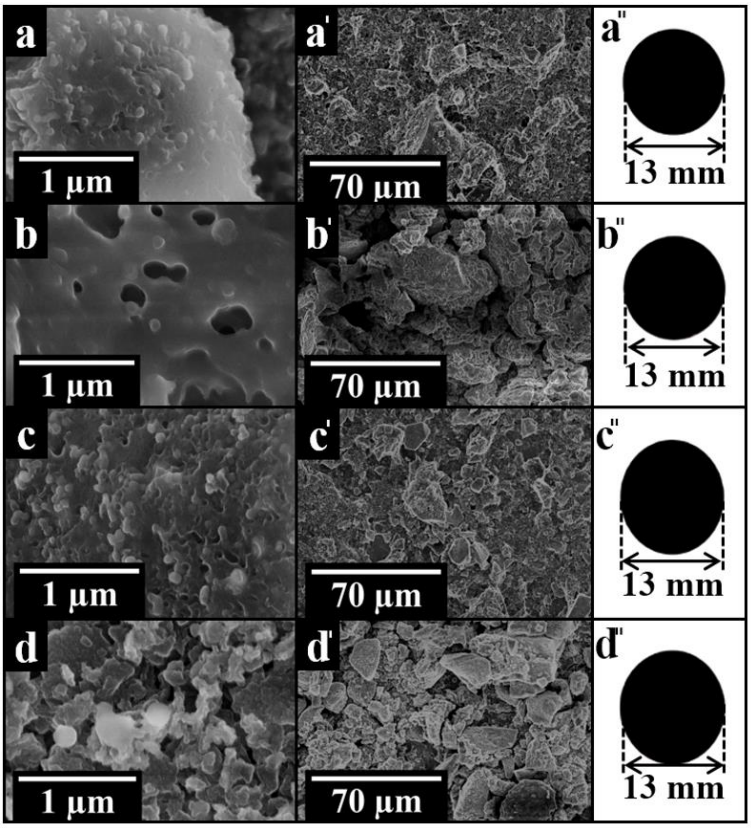

Figure 13. SEM images (a, a′, b, b′, c, c′, d and d′) and photo microscopic images (a″, b″, c″, and d″) of the Si/C (a, a′, a″, b, b′, b″) and Si/Ag/C (c, c′, c″, d, d′, d″) nanohybrid electrodes. Image a, a′, a″, c, c′ and c″ refer to the electrode morphology before cycling. Images b, b′, b″, d, d′ and d″ refer to the electrode morphology after 100 cycles.

Conclusions

A concept has been developed to improve the electrochemical performance of the silicon based lithium-ion battery anode by homogeneously incorporating the super-small metal nanoparticles into the Si/C composite, as demonstrated by the Si/Ag/C nanohybrid anode. By using epoxy resin monomer as solvent for silicon particle dispersion and carbon source, super-small silver nanoparticles are *in situ* synthesized and homogeneously embedded into the *in situ* formed nitrogen-doped carbon matrix. The curing agent DETA is applied to dissolve silver nitrate and introduce the dissolved silver species into the epoxy resin solution. Upon polymerization, both Si

nanoparticles and silver species are incorporated into the thermosetting epoxy polymer network. Through calcination in argon atmosphere at 800 °C, super-small silver nanoparticles with the average diameter of 2.9 nm are *in situ* synthesized and the thermosetting epoxy polymer is simultaneously transformed into a continuous nitrogen doped carbon matrix. The structure, morphology, crystallinity, and porosity of the Si/C and Si/Ag/C nanohybrids are systematically investigated by XRD, Raman, FTIR, TGA, TEM, EDX, nitrogen adsorption-desorption measurement, XPS, and SAXS. The electrochemical performance of the Si/C and Si/Ag/C nanohybrid as lithium-ion battery anodes are tested. A significant rate performance improvement is achieved with incorporation of tiny amount of the super-small silver nanoparticles (2.59 % by mass). The existence of the super-small silver nanoparticles effectively enhances the electron transportation within the electrode as confirmed by both EIS measurement and theoretical calculation. The mechanism for the enhanced rate performance is also investigated by uncovering the temperature dependent electron conductivity behavior of the Si/Ag/C nanohybrids with different silver concentrations. It proves that the incorporation of the super-small silver nanoparticles in the carbon matrix leads to a significantly enhanced charge carrier mobility. Besides the rate performance, the Si/Ag/C nanohybrid also exhibits slightly improved cyclic stability that the Si/C sample. The Si nanoparticles are well embedded in the buffer medium of continuous carbon matrix containing silver nanoparticles. The tremendous amounts of super-small silver nanoparticles with excellent mechanical properties may act as stress absorption centers to help stabilize the electrode upon drastic volume change. The work presented in this manuscript is in principle universally applicable to other metal system and provide a way to improve the electrochemical performance of the silicon based lithium-ion battery anode with tiny amount of metal species.

METHODS

Materials

All chemicals were used as received without further purification. $AgNO_3$ (99.8 %) were purchased from Aladdin Reagent Co., Ltd., Shanghai, China. Silicon nanoparticles (30 nm, 99.9 %) were bought from HT-NANO Shanghai, China. Diethylenetriamine (DETA, ≥ 98 %) was obtained from Damao Chemical Reagent, Tianjin, China. Epoxy resin (DER331) was purchased from DOW. USA. Sodium alginate was obtained from Aladdin Reagent Co., Ltd., China. Conductive carbon Super P was bought from SCM Chem. Shanghai, China.

Sample Synthesis

The synthesis of the Si/Ag/C nanohybrid is described as follows: $AgNO_3$ (0.3 gram) was dissolved in DETA (diethylenetriamine, 1.47 gram) through ultrasonication (60 W, 2 h) at room temperature until a clear light yellow solution was observed. Meanwhile, Si nanoparticles (1 gram) were dispersed in an epoxy resin solution (DER331, 10 gram) with stirring at 80 $^{\circ}$C to form a homogeneous suspension. Thereafter, the curing agent solution containing $AgNO_3$ and DETA was poured into the Si/DER 331 suspension accompanied by manual stirring at room temperature to keep homogeneous dispersion. The mixture was then transferred to a PTFE mould, followed by polymerization at 80 $^{\circ}$C for 30 minutes. The as-polymerized composites were smashed into small particulate powders with a mixer. Calcination in argon atmosphere was performed at 800 $^{\circ}$C for 4 hours in a tube furnace with a ramp rate of 5 K/min starting from room temperature, followed by natural cooling to room temperature. The calcined samples were then ball milled with a planetary ball miller (FRITSCH-pulverisette 7, Germany) for 4 hours with the speed of 400 rpm, followed by sieving with a 300 mesh sieve. The control sample of the Si/C nanohybrid was prepared with the

same protocol except no silver nitrate was used. The Si/Ag/C nanohybrids with different silver compositions were synthesized with similar protocols where the feeding amount of the silver nitrate was tuned. The exact amount of the diethylenetriamine used was calculated based on the epoxy value of the epoxy resin.[47]

Sample Characterization

The curing degree of the epoxy resin was evaluated with soxhlet extraction in acetone, which was performed at 100 °C for 48 hours. X-ray diffraction (XRD) characterization was performed on a diffractometer (Bruker AXS D8 Advance, λ = 1.541 Å, 2.2 kW) with 2 theta range from 5 ° to 90 °. The EDX elemental mapping was carried out with FEI QUANTA 250 FEG (America FEI) at an accelerating voltage of 15 kV. The microstructure images of the electrodes were obtained with Hitachi S4800 scanning electron microscope (Tokyo, Japan) at an accelerating voltage of 4 kV. TEM experiment was performed with a JEOL JEM-2100F TEM or Tecnai F20 (America FEI) instrument operated at 200 kV. The specific surface area measurement was carried out based on N_2 adsorption desorption test with Micromeritics ASAP2020 Accelerated Surface Area and Porosimetry System. The carbon contents of the samples were determined by a thermogravimetric analyzer (TGA, Mettler Toledo, Switzerland) in air atmosphere, the temperature range was set between 50 ℃ and 800 ℃ and the ramp rate was 20 K/min. Raman spectroscopy was collected on a Renishaw (in Via-reflex) with the excitation wavelength of 532 nm. Fourier transform infrared (FTIR) analysis was performed on a Nicolet 6700 infrared spectrometer. The spectra (4000 cm^{-1} - 400 cm^{-1}) were recorded with a resolution of 0.9 cm^{-1} and 32 scans per sample. The silver content in Si/Ag/C nanohybrid was measured by inductively coupled plasma optical emission spectrometer (ICP-OES, Perkin-Elmer, USA). Specifically, 0.01 g of the Si/Ag/C power was added to a digestion

high-pressure tank with 8 ml HCl (36 % - 38 %), 0.5 ml $HClO_4$ (70 % - 72 %), 0.5 ml H_2O_2 (≥ 30 %) and 0.5 ml HF (≥ 40 %). The digestion process was performed at 180 ℃ for 4 h. Small-angle X-ray scattering (SAXS) measurements were performed using a Ganesha 300XL SAXS−WAXS system (SAXS LAB ApS, Copenhagen/Denmark) with an X-ray wavelength of 0.154 nm. The detector was positioned at a distance of 406 mm from the sample. Glass capillaries were used as sample containers for the SAXS measurements. X-ray photoelectron spectroscopy (XPS) measurement was done with an ESCALAB 250Xi spectrometer, using focused monochromatized Al Kα radiation (hν = 1486.6 eV) at room temperature. I-V measurement was carried out on Physical Property Measurement System (Model 9, USA) with a temperature range between 100 K and 300 K. The test current was 0.1 mA and frequency was 60 Hz. The silver paste (H20E silver epoxy) used on connecting wires was brought from EPO-TEK Co., Ltd. 0.1 g active material and 1.0 g KBr were fully mixed and ground in an agate mortar. Thereafter, the mixture powder was pressed into a pellet using an infrared press machine with a pressure of 20 MPa. The pellet was carved into a rectangular shape of 7 mm × 2 mm.

Electrode Fabrication

The active material, sodium alginate, and super P were thoroughly mixed together in mortar with a composition of 7:2:1 by mass in water. Thereafter, the slurry was spread onto a copper foil by doctor blading, followed by drying in oven at 40 °C for 4 hours. After drying the copper foil was pressed, and cut into spherical electrodes with the diameter of 13 mm. The actual mass loading of the active material on different electrodes are listed in **Table 2**. The mass loaded on the copper foil was weighed using a balance with a resolution of 0.01 mg. After weighing, the electrodes were stored in oven at 80 °C for 4 hours before coin cell assembly. Coin type cells (CR2032) were

assembled in a glove box (MB-10-compact, MBRAUN) filled with Argon. The oxygen and water contents were monitored to be less than 0.5 ppm. Li metal foil was applied as counter electrode and Celgard 2300 was used as separator respectively. Commercial electrolyte from Dongguan Shanshan Co., Ltd was used, where 1 M $LiPF_6$ was dissolved in a mixture of ethylene carbonate (EC) and diethyl carbonate (DEC) with a volume ratio of 1:1. After assembly the coin cells were aged for 24 hours before electrochemical performance test.

Table 2. Mass loading density of the electrodes with respect to the active material.

Testing condition	mass loading density of the active material $mgcm^{-2}$	
	Si/C electrode ($m_{Si/C}$)	Si/Ag/C electrode ($m_{Si/Ag/C}$)
cycling performance test	1.32	1.13
rate performance test	1.25	1.21

Electrochemical Test

The cells were discharged and charged on a battery tester (LAND2001A, China) between 0.005 V and 3.0 V (vs. Li/Li^+) with a current density of 0.2 C (1 C = 1000 mA g^{-1}) at room temperature. The rate performance was measured at a current density sequence of 0.1 C, 0.2 C, 0.5 C, 1.0 C and 0.1 C in the voltage range between 0.005 V and 3.0 V (vs Li/Li^+) (five cycles each current density). The lithiation process was defined as discharge process and the corresponding delithiation process was indexed as charge process. The electrochemical impedance spectroscopy (EIS) measurements were performed over a frequency range from 10 kHz to 0.001 Hz. The CHI 1040B potentiostat/galvanostat analyzer (Shanghai Chenhua instrument Co., Ltd.) was used to conduct the cyclic voltammetry test at a scanning rate of 0.2 mV/s with the voltage range between 0.001 V and 3.0 V. It is reported that the lithiation of silver mainly occurs below 0.07 V and the alloying/de-alloying process between Ag and Li is difficult.[37, 78] Therefore the lithiation of the silver

nanoparticles during the repeated cycling is neglected. The specific capacity is calculated based on the mass of the Si and carbon content in both samples.

ASSOCIATED CONTENT

Supporting Information

The Supporting Information is available free of charge on the ACS publications website. I-V curves of the Si/Ag/C nanohybrids with different silver compositions.

AUTHOR INFORMATION

Corresponding Author

*E-mail: chengyj@nimte.ac.cn

ORCID

Yonggao Xia: 0000-0003-4901-1176

Ya-Jun Cheng: 0000-0002-0932-295X

Notes

The authors declare no competing financial interest.

Acknowledgement

The authors would like to thank Prof. Dr. Xile Hu for the fruitful scientific discussions. This research is funded by the National Key R&D Program of China (Grant No. 2016YFB0100100), Natural Science Foundation of China (51103172, 51702335), the Zhejiang Nonprofit Technology Applied Research Program (2013C33190), and the open project of the Beijing National Laboratory for Molecular Science (20140138), the CAS-EU S&T cooperation partner program (174433KYSB20150013) and Key Laboratory of Bio-based Polymeric Materials of Zhejiang Province. S.X. acknowledges the China Scholarship Council (CSC) and P.M-B acknowledges

funding by the International Research Training Group 2022 Alberta/Technical University of Munich International Graduate School for Environmentally Responsible Functional Hybrid Materials (ATUMS).

References

1. Armand, M.; Tarascon, J. M. Building Better Batteries. *Nature* **2008,** *451*, 652-657.
2. Chen, T.; Qiu, L.; Yang, Z.; Cai, Z.; Ren, J.; Li, H.; Lin, H.; Sun, X.; Peng, H. An Integrated "Energy Wire" for Both Photoelectric Conversion and Energy Storage. *Angew. Chem., Int. Ed.* **2012,** *51*, 11977-11980.
3. Roy, P.; Srivastava, S. K. Nanostructured Anode Materials for Lithium Ion Batteries. *J. Mater. Chem. A* **2015,** *3*, 2454-2484.
4. Park, D.-W.; Jeong, Y.; PremKumar, T.; Lee, J. Quasi-Photonic Crystal Effect of Ticl3/Electrolyte Matrix in Unipolar Dye-Absorber Devices. *ACS Appl. Mater. Interfaces* **2014,** *6*, 14399-14404.
5. Tollefson, J. Car Industry: Charging up the Future. *Nature* **2008,** *456*, 436-440.
6. Dunn, B.; Kamath, H.; Tarascon, J.-M. Electrical Energy Storage for the Grid: A Battery of Choices. *Science* **2011,** *334*, 928-935.
7. Kim, J. W.; Ocon, J. D.; Park, D.-W.; Lee, J. Functionalized Graphene-Based Cathode for Highly Reversible Lithium-Sulfur Batteries. *ChemSusChem* **2014,** *7*, 1265-1273.
8. Kaskhedikar, N. A.; Maier, J. Lithium Storage Ion Carbon Nanostructures. *Adv. Mater.***2009,** *21*, 2664-2680.
9. Szczech, J. R.; Jin, S. Nanostructured Silicon for High Capacity Lithium Battery Anodes. *Energy Environ. Sci.* **2011,** *4*, 56-72.
10. Ge, M.; Fang, X.; Rong, J.; Zhou, C. Review of Porous Silicon Preparation and Its Application for Lithium-Ion Battery Anodes. *Nanotechnology* **2013,** *24*.
11. Zamfir, M. R.; Hung Tran, N.; Moyen, E.; Lee, Y. H.; Pribat, D. Silicon Nanowires for Li-Based Battery Anodes: A Review. *J. Mater. Chem. A* **2013,** *1*, 9566-9586.
12. Su, X.; Wu, Q.; Li, J.; Xiao, X.; Lott, A.; Lu, W.; Sheldon, B. W.; Wu, J. Silicon-Based Nanomaterials for Lithium-Ion Batteries: A Review. *Adv. Energy Mater.* **2014,** *4*.
13. Kim, N.; Chae, S.; Ma, J.; Ko, M.; Cho, J. Fast-Charging High-Energy Lithium-Ion Batteries Via Implantation of Amorphous Silicon Nanolayer in Edge-Plane Activated Graphite Anodes. *Nat. Commun.* **2017,** *8*.
14. Pietsch, P.; Westhoff, D.; Feinauer, J.; Eller, J.; Marone, F.; Stampanoni, M.; Schmidt, V.; Wood, V. Quantifying Microstructural Dynamics and Electrochemical Activity of Graphite and Silicon-Graphite Lithium Ion Battery Anodes. *Nat. Commun.* **2016,** *7*.
15. Xiao, Q.; Gu, M.; Yang, H.; Li, B.; Zhang, C.; Liu, Y.; Liu, F.; Dai, F.; Yang, L.; Liu, Z.; Xiao, X.; Liu, G.; Zhao, P.; Zhang, S.; Wang, C.; Lu, Y.; Cai, M. Inward Lithium-Ion Breathing of Hierarchically Porous Silicon Anodes. *Nat. Commun.* **2015,** *6*.
16. Wang, X.; Fan, F.; Wang, J.; Wang, H.; Tao, S.; Yang, A.; Liu, Y.; Chew, H. B.; Mao, S. X.; Zhu, T.; Xia, S. High Damage Tolerance of Electrochemically Lithiated Silicon. *Nat. Commun.* **2015,** *6*.
17. Piper, D. M.; Evans, T.; Leung, K.; Watkins, T.; Olson, J.; Kim, S. C.; Han, S. S.; Bhat, V.; Oh, K. H.; Buttry, D. A.; Lee, S.-H. Stable Silicon-Ionic Liquid Interface for Next-Generation Lithium-Ion Batteries. *Nat. Commun.* **2015,** *6*.
18. Li, X.; Gu, M.; Hu, S.; Kennard, R.; Yan, P.; Chen, X.; Wang, C.; Sailor, M. J.; Zhang, J.-G.; Liu, J. Mesoporous Silicon Sponge as an Anti-Pulverization Structure for High-Performance Lithium-Ion Battery Anodes. *Nat. Commun.* **2014,** *5*.
19. Wu, H.; Yu, G.; Pan, L.; Liu, N.; McDowell, M. T.; Bao, Z.; Cui, Y. Stable Li-Ion Battery Anodes by in-Situ Polymerization of Conducting Hydrogel to Conformally Coat Silicon Nanoparticles. *Nat.*

Commun. **2013,** *4*.
20. Liu, X. H.; Zhong, L.; Huang, S.; Mao, S. X.; Zhu, T.; Huang, J. Y. Size-Dependent Fracture of Silicon Nanoparticles During Lithiation. *ACS Nano* **2012,** *6*, 1522-1531.
21. Shi, F.; Song, Z.; Ross, P. N.; Somorjai, G. A.; Ritchie, R. O.; Komvopoulos, K. Failure Mechanisms of Single-Crystal Silicon Electrodes in Lithium-Ion Batteries. *Nat. Commun.* **2016,** *7*.
22. Lee, S. W.; Lee, H.-W.; Ryu, I.; Nix, W. D.; Gao, H.; Cui, Y. Kinetics and Fracture Resistance of Lithiated Silicon Nanostructure Pairs Controlled by Their Mechanical Interaction. *Nat. Commun.* **2015,** *6*.
23. Wu, H.; Cui, Y. Designing Nanostructured Si Anodes for High Energy Lithium Ion Batteries. *Nano Today* **2012,** *7*, 414-429.
24. Li, Y. Z.; Yan, K.; Lee, H. W.; Lu, Z. D.; Liu, N.; Cui, Y. Growth of Conformal Graphene Cages on Micrometre-Sized Silicon Particles as Stable Battery Anodes. *Nat. Energy* **2016,** *1*.
25. Zuo, X.; Zhu, J.; Müller-Buschbaum, P.; Cheng, Y.-J. Silicon Based Lithium-Ion Battery Anodes: A Chronicle Perspective Review. *Nano Energy* **2017,** *31*, 113-143.
26. Song, J.; Chen, S.; Zhou, M.; Xu, T.; Lv, D.; Gordin, M. L.; Long, T.; Melnyk, M.; Wang, D. Micro-Sized Silicon-Carbon Composites Composed of Carbon-Coated Sub-10 Nm Si Primary Particles as High-Performance Anode Materials for Lithium-Ion Batteries. *J. Mater. Chem. A* **2014,** *2*, 1257-1262.
27. Kim, H.; Seo, M.; Park, M.-H.; Cho, J. A Critical Size of Silicon Nano-Anodes for Lithium Rechargeable Batteries. *Angew. Chem., Int. Ed.* **2010,** *49*, 2146-2149.
28. Ni, S.; Lv, X.; Li, T.; Yang, X.; Zhang, L.; Ren, Y. A Novel Electrochemical Activation Effect Induced Morphology Variation from Massif-Like Cuxo to Forest-Like Cu2o Nanostructure and the Excellent Electrochemical Performance as Anode for Li-Ion Battery. *Electrochim. Acta* **2013,** *96*, 253-260.
29. Hou, X.; Zhang, M.; Wang, J.; Hu, S.; Liu, X. Deposition of Silver Nanoparticles into Silicon/Carbon Composite as a High-Performance Anode Material for Li-Ion Batteries. *J. Solid State Electrochem.* **2015,** *19*, 3595-3604.
30. Zhang, F.; Yang, X.; Xie, Y.; Yi, N.; Huang, Y.; Chen, Y. Pyrolytic Carbon-Coated Si Nanoparticles on Elastic Graphene Framework as Anode Materials for High-Performance Lithium-Ion Batteries. *Carbon* **2015,** *82*, 161-167.
31. Wang, B.; Li, X.; Zhang, X.; Luo, B.; Jin, M.; Liang, M.; Dayeh, S. A.; Picraux, S. T.; Zhi, L. Adaptable Silicon-Carbon Nanocables Sandwiched between Reduced Graphene Oxide Sheets as Lithium Ion Battery Anodes. *ACS Nano* **2013,** *7*, 1437-1445.
32. Yu, J.; Zhan, H.; Wang, Y.; Zhang, Z.; Chen, H.; Li, H.; Zhong, Z.; Su, F. Graphite Microspheres Decorated with Si Particles Derived from Waste Solid of Organosilane Industry as High Capacity Anodes for Li-Ion Batteries. *J. Power Sources* **2013,** *228*, 112-119.
33. Wang, W.; Kumta, P. N. Nanostructured Hybrid Silicon/Carbon Nanotube Heterostructures: Reversible High-Capacity Lithium-Ion Anodes. *ACS Nano* **2010,** *4*, 2233-2241.
34. Tao, H.; Fan, L.-Z.; Song, W.-L.; Wu, M.; He, X.; Qu, X. Hollow Core-Shell Structured Si/C Nanocomposites as High-Performance Anode Materials for Lithium-Ion Batteries. *Nanoscale* **2014,** *6*, 3138-3142.
35. Yang, X.; Wen, Z.; Huang, S.; Zhu, X.; Zhang, X. Electrochemical Performances of Silicon Electrode with Silver Additives. *Solid State Ionics* **2006,** *177*, 2807-2810.
36. Ohara, S.; Suzuki, J.; Sekine, K.; Takamura, T. Li Insertion/Extraction Reaction at a Si Film Evaporated on a Ni Foil. *J. Power Sources* **2003,** *119-121*, 591-596.

37. Talla, G.; Guduru, R. K.; Li, B. Q.; Mohanty, P. S. Doped-Si–Ag Composite Electrodes for Li-Ion Batteries. *Solid State Ionics* **2015,** *269*, 8-13.
38. Liu, Y.; Chen, B.; Cao, F.; Chan, H. L. W.; Zhao, X.; Yuan, J. One-Pot Synthesis of Three-Dimensional Silver-Embedded Porous Silicon Micronparticles for Lithium-Ion Batteries. *J. Mater. Chem.* **2011,** *21*, 17083.
39. Cheng, Y.; Yi, Z.; Wang, C. L.; Wang, L. D.; Wu, Y. M.; Wang, L. M. Influence of Copper Addition for Silicon-Carbon Composite as Anode Materials for Lithium Ion Batteries. *RSC Adv.* **2016,** *6*, S6756-S6764.
40. Wang, N.; Hang, T.; Ling, H. Q.; Hu, A. M.; Li, M. High-Performance Si-Based 3d Cu Nanostructured Electrode Assembly for Rechargeable Lithium Batteries. *J. Mater. Chem. A* **2015,** *3*, 11912-11919.
41. Meng, X. H.; Deng, D. Core-Shell Ti@Si Coaxial Nanorod Arrays Formed Directly on Current Collectors for Lithium-Ion Batteries. *ACS Appl. Mater. Interfaces* **2015,** *7*, 6867-6874.
42. Zhao, W. J.; Du, N.; Xiao, C. M.; Wu, H.; Zhang, H.; Yang, D. R. Large-Scale Synthesis of Ag-Si Core-Shell Nanowall Arrays as High-Performance Anode Materials of Li-Ion Batteries. *J. Mater. Chem. A* **2014,** *2*, 13949-13954.
43. Chen, D.; Mei, X.; Ji, G.; Lu, M.; Xie, J.; Lu, J.; Lee, J. Y. Reversible Lithium-Ion Storage in Silver-Treated Nanoscale Hollow Porous Silicon Particles. *Angew. Chem., Int. Ed.* **2012,** *51*, 2409-2413.
44. Cao, F. F.; Deng, J. W.; Xin, S.; Ji, H. X.; Schmidt, O. G.; Wan, L. J.; Guo, Y. G. Cu-Si Nanocable Arrays as High-Rate Anode Materials for Lithium-Ion Batteries. *Adv. Mater.***2011,** *23*, 4415-+.
45. Zhang, S. C.; Du, Z. J.; Lin, R. X.; Jiang, T.; Liu, G. R.; Wu, X. M.; Weng, D. S. Nickel Nanocone-Array Supported Silicon Anode for High-Performance Lithium-Ion Batteries. *Adv. Mater.***2010,** *22*, 5378-+.
46. Yu, Y.; Gu, L.; Zhu, C.; Tsukimoto, S.; van Aken, P. A.; Maier, J. Reversible Storage of Lithium in Silver-Coated Three-Dimensional Macroporous Silicon. *Adv. Mater.***2010,** *22*, 2247-+.
47. Kim, J. W.; Ryu, J. H.; Lee, K. T.; Oh, S. M. Improvement of Silicon Powder Negative Electrodes by Copper Electroless Deposition for Lithium Secondary Batteries. *J. Power Sources* **2005,** *147*, 227-233.
48. Cheng, Y.-J.; Zeiger, D. N.; Howarter, J. A.; Zhang, X.; Lin, N. J.; Antonucci, J. M.; Lin-Gibson, S. In Situ Formation of Silver Nanoparticles in Photocrosslinking Polymers. *J. Biomed. Mater. Res., Part B* **2011,** *97B*, 124-131.
49. Tang, H.; Xia, X. H.; Zhang, Y. J.; Tong, Y. Y.; Wang, X. L.; Gu, C. D.; Tu, J. P. Binary Conductive Network for Construction of Si/Ag Nanowires/Rgo Integrated Composite Film by Vacuum-Filtration Method and Their Application for Lithium Ion Batteries. *Electrochim. Acta* **2015,** *180*, 1068-1074.
50. Kwon, E.; Lim, H.-S.; Sun, Y.-K.; Suh, K.-D. Improved Rate Capability of Lithium-Ion Batteries with Ag Nanoparticles Deposited onto Silicon/Carbon Composite Microspheres as an Anode Material. *Solid State Ionics* **2013,** *237*, 28-33.
51. Su, M.; Wang, Z.; Guo, H.; Li, X.; Huang, S.; Xiao, W.; Gan, L. Enhancement of the Cyclability of a Si/Graphite@Graphene Composite as Anode for Lithium-Ion Batteries. *Electrochim. Acta* **2014,** *116*, 230-236.
52. Xiao, Y.; Wang, X. Y.; Xia, Y. G.; Yao, Y.; Metwalli, E.; Zhang, Q.; Liu, R.; Qiu, B.; Rasool, M.; Liu, Z. P.; Meng, J. Q.; Sun, L. D.; Yan, C. H.; Mueller-Buschbaum, P.; Cheng, Y. J. Green Facile Scalable Synthesis of Titania/Carbon Nanocomposites: New Use of Old Dental Resins. *ACS Appl. Mater.*

Interfaces **2014,** *6*, 18461-18468.
53. Wang, X.; Meng, J. Q.; Wang, M.; Xiao, Y.; Liu, R.; Xia, Y.; Yao, Y.; Metwalli, E.; Zhang, Q.; Qiu, B.; Liu, Z.; Pan, J.; Sun, L. D.; Yan, C. H.; Muller-Buschbaum, P.; Cheng, Y. J. Facile Scalable Synthesis of Tio2/Carbon Nanohybrids with Ultrasmall Tio2 Nanoparticles Homogeneously Embedded in Carbon Matrix. *ACS Appl Mater Interfaces* **2015,** *7*, 24247-55.
54. Wang, M.; Xia, Y.; Wang, X.; Xiao, Y.; Zhang, Q.; Liu, R.; Qiu, B.; Wu, Q.; Chen, G.; Liu, Y.; Yang, Z.; Liu, Z.; Meng, J. Q.; Sun, L. D.; Yan, C. H.; Pan, J.; Cheng, Y. J. Facile Scalable Synthesis of Sioc/Carbon Nanohybrids as Lithium-Ion Battery Anode Inspired by Dental Restorative Materials. *Dig J Nanomater Bios* **2016,** *11*, 567-578.
55. Wang, M.; Xia, Y.; Wang, X.; Xiao, Y.; Liu, R.; Wu, Q.; Qiu, B.; Metwalli, E.; Xia, S.; Yao, Y.; Chen, G.; Liu, Y.; Liu, Z.; Meng, J. Q.; Yang, Z.; Sun, L. D.; Yan, C. H.; Muller-Buschbaum, P.; Pan, J.; Cheng, Y. J. Silicon Oxycarbide/Carbon Nanohybrids with Tiny Silicon Oxycarbide Particles Embedded in Free Carbon Matrix Based on Photoactive Dental Methacrylates. *ACS Appl Mater Interfaces* **2016,** *8*, 13982-92.
56. Li, W.; Cao, K.; Wang, H.; Liu, J.; Zhou, L.; Yao, H. Carbon Coating May Expedite the Fracture of Carbon-Coated Silicon Core-Shell Nanoparticles During Lithiation. *Nanoscale* **2016,** *8*, 5254-9.
57. Faria, A. F.; Martinez, D. S. T.; Moraes, A. C. M.; Maia da Costa, M. E. H.; Barros, E. B.; Souza Filho, A. G.; Paula, A. J.; Alves, O. L. Unveiling the Role of Oxidation Debris on the Surface Chemistry of Graphene through the Anchoring of Ag Nanoparticles. *Chem. Mater.* **2012,** *24*, 4080-4087.
58. Zhou, W.; Upreti, S.; Whittingham, M. S. Electrochemical Performance of Al-Si-Graphite Composite as Anode for Lithium-Ion Batteries. *Electrochem. Commun.* **2011,** *13*, 158-161.
59. Wang, Y.; Su, F.; Wood, C. D.; Lee, J. Y.; Zhao, X. S. Preparation and Characterization of Carbon Nanospheres as Anode Materials in Lithium-Ion Secondary Batteries. *Ind. Eng. Chem. Res.* **2008,** *47*, 2294-2300.
60. Deshmukh, P.; Peshwe, D.; Pathak, S. FTIR and TGA Analysis in Relation with the % Crystallinity of the SiO_2 Obtained by Burning Rice Husk at Various Temperatures. *Adv. Mater. Res* **2012,** *585*, 77-81.
61. Ban, J.; Yang, P.; Xiaa, Y.; Wang, M.; Wang, X.; Xiao, Y.; Qiu, B.; Yang, L.; Liu, Z.; Zhu, C.; Chen, C.; Cheng, Y. J. Facile Synthesis of Mno/Carbon/Carbon Nanotube Nanohybrids Using Dental Resins as Solvent and Carbon Source. *Dig J Nanomater Bios* **2016,** *11*, 223-234.
62. Wang, L.; Dou, S.; Xu, J. T.; Liu, H. K.; Wang, S. Y.; Ma, J. M.; Dou, S. X. Highly Nitrogen Doped Carbon Nanosheets as an Efficient Electrocatalyst for the Oxygen Reduction Reaction. *Chem. Commun.* **2015,** *51*, 11791-11794.
63. Li, X.; Feng, Y.; Li, M.; Li, W.; Wei, H.; Song, D. Smart Hybrids of Zn2geo4nanoparticles and Ultrathin G-C3n4layers: Synergistic Lithium Storage and Excellent Electrochemical Performance. *Adv. Funct. Mater.* **2015,** *25*, 6858-6866.
64. Sheng, Z. H.; Shao, L.; Chen, J. J.; Bao, W. J.; Wang, F. B.; Xia, X. H. Catalyst-Free Synthesis of Nitrogen-Doped Graphene Via Thermal Annealing Graphite Oxide with Melamine and Its Excellent Electrocatalysis. *ACS Nano* **2011,** *5*, 4350-4358.
65. Li, J.; Dahn, J. R. An in Situ X-Ray Diffraction Study of the Reaction of Li with Crystalline Si. *J. Electrochem. Soc.* **2007,** *154*, A156-A161.
66. Du, F.-H.; Wang, K.-X.; Fu, W.; Gao, P.-F.; Wang, J.-F.; Yang, J.; Chen, J.-S. A Graphene-Wrapped Silver-Porous Silicon Composite with Enhanced Electrochemical Performance for Lithium-Ion

Batteries. *J. Mater. Chem. A* **2013,** *1*, 13648-13654.
67. Obrovac, M. N.; Krause, L. J. Reversible Cycling of Crystalline Silicon Powder. *J. Electrochem. Soc.* **2007,** *154*, A103-A108.
68. Xiao, W.; Wang, Z.; Guo, H.; Li, X.; Wang, J.; Huang, S.; Gan, L. Fe2o3 Particles Enwrapped by Graphene with Excellent Cyclability and Rate Capability as Anode Materials for Lithium Ion Batteries. *Appl. Surf. Sci.* **2013,** *266*, 148-154.
69. Liu, Y.; Hanai, K.; Yang, J.; Imanishi, N.; Hirano, A.; Takeda, Y. Morphology-Stable Silicon-Based Composite for Li-Intercalation. *Solid State Ionics* **2004,** *168*, 61-68.
70. Kong, J.; Yee, W. A.; Wei, Y.; Yang, L.; Ang, J. M.; Phua, S. L.; Wong, S. Y.; Zhou, R.; Dong, Y.; Li, X.; Lu, X. Silicon Nanoparticles Encapsulated in Hollow Graphitized Carbon Nanofibers for Lithium Ion Battery Anodes. *Nanoscale* **2013,** *5*, 2967-2973.
71. Kim, H.; Cho, J. Superior Lithium Electroactive Mesoporous Si@Carbon Core-Shell Nanowires for Lithium Battery Anode Material. *Nano Lett.* **2008,** *8*, 3688-3691.
72. Limthongkul, P.; Jang, Y. I.; Dudney, N. J.; Chiang, Y. M. Electrochemically-Driven Solid-State Amorphization in Lithium-Silicon Alloys and Implications for Lithium Storage. *Acta Mater.* **2003,** *51*, 1103-1113.
73. Yoo, S.; Lee, J. I.; Ko, S.; Park, S. Highly Dispersive and Electrically Conductive Silver-Coated Si Anodes Synthesized Via a Simple Chemical Reduction Process. *Nano Energy* **2013,** *2*, 1271-1278.
74. Gu, M.; Ko, S.; Yoo, S.; Lee, E.; Min, S. H.; Park, S.; Kim, B.-S. Double Locked Silver-Coated Silicon Nanoparticle/Graphene Core/Shell Fiber for High-Performance Lithium-Ion Battery Anodes. *J. Power Sources* **2015,** *300*, 351-357.
75. Jiang, T.; Zhang, S.; Qiu, X.; Zhu, W.; Chen, L. Preparation and Characterization of Silicon-Based Three-Dimensional Cellular Anode for Lithium Ion Battery. *Electrochem. Commun.* **2007,** *9*, 930-934.
76. Zhang, Y. B.; Small, J. P.; Pontius, W. V.; Kim, P. Fabrication and Electric-Field-Dependent Transport Measurements of Mesoscopic Graphite Devices. *Appl. Phys. Lett.* **2005,** *86*.
77. Klein, C. A. Stb Model + Transport Properties of Pyrolytic Graphites. *J. Appl. Phys.* **1964,** *35*, 2947-&.
78. Hwang, S. M.; Lee, H. Y.; Jang, S. W.; Lee, S. M.; Lee, S. J.; Baik, H. K.; Lee, J. Y. Lithium Insertion in Siag Powders Produced by Mechanical Alloying. *Electrochem. Solid-State Lett.* **2001,** *4*, A97-A100.

Table of Content

Super-small silver nanoparticles with an average diameter of 2.9 nm are *in situ* synthesized and homogeneously embedded in the Si/C nanohybrid, using epoxy resin as solvent and carbon source. Superior rate performance and improved cyclic stability are achieved with tiny amount of silver (2.59 % by mass).